2021

Multiscale Finite Element Modeling of Active Contraction in Striated Muscle

Charles Kurtis Mann

University of Kentucky, charlesk.mann@gmail.com
Author ORCID Identifier:
https://orcid.org/0000-0001-6603-9037
Digital Object Identifier: https://doi.org/10.13023/etd.2021.321

MULTISCALE FINITE ELEMENT MODELING OF ACTIVE CONTRACTION IN
STRIATED MUSCLE

_____

DISSERTATION
_____

A dissertation submitted in partial fulfillment of the
requirements for the degree of Doctor of Philosophy in
the College of Engineering at the University of
Kentucky
By
Charles Kurtis Mann

Lexington, Kentucky

Director: Dr. Jonathan F. Wenk, Professor of Mechanical Engineering

Lexington, Kentucky

2021

ABSTRACT OF DISSERTATION

MULTISCALE FINITE ELEMENT MODELING OF ACTIVE CONTRACTION IN
STRIATED MUSCLE

Greater than one in three American adults have at least one type of cardiovascular
disease, a major cause of morbidity. Computational cardiac mechanics has become an
important part of the research effort to understand the heart's response to mechanical
stimuli and as an extension, disease progression and potential therapies. To this end, the
present work aims to extend these efforts by implementing a cell level contractile model
in which active stress generation in muscle tissue is driven by half-sarcomere
mechanics. This is accomplished by enhancing the MyoSim model of actin and myosin
in order to produce a multiscale model. This contraction model simulates cross-bridge
dynamics and captures key components of contraction such as length-dependent
activation, Ca2+ activation and sensitivity, and filament cooperativity. Embedding this
physiologically motivated contraction model allows for the testing of hypotheses and
predictions regarding the interplay between molecular mechanisms and organ level
function, while capturing spatial heterogeneity. This multiscale approach has been
used to predict an increase in the end-systolic pressure-volume relationship due to the
inclusion of a recently discovered super-relaxed state in left-ventricle simulations. It has
also been used to predict a decrease in stress generation and efficiency in skeletal
muscles due to myofibril misalignment. Finally, the foundation for cardiac growth and
remodeling simulations has been implemented.

KEYWORDS: Cardiac Mechanics, Finite Element Modeling, Multiscale Modeling,
Sarcomere Kinetics, Continuum Mechanics

Charles Kurtis Mann

07/28/2021
Date

MULTISCALE FINITE ELEMENT MODELING OF ACTIVE CONTRACTION IN
STRIATED MUSCLE

By

Charles Kurtis Mann

Jonathan F. Wenk
Director of Dissertation

Alexandre Martin
Director of Graduate Studies

07/28/2021
Date

To my wife Jamie, and my son Charlie

ACKNOWLEDGEMENTS

TABLE OF CONTENTS

LIST OF TABLES

LIST OF FIGURES

CHAPTER 1: INTRODUCTION

The heart can be viewed as one of the most mechanical organs of the body. As a most basic description, it can be described as a simple pump. However, close examination of myocardial tissue reveals a complex network of constituents including striated muscle cells aligned in fibers, a complex collagen fiber matrix, fluid and other biological components. The size of these constituents bridge various length scales, and the processes that drive cardiac function span various time scales, with disease states being considered over long time courses. Cardiac function can be analyzed through multiple lenses, for example mechanical, electrical, hormonal, etc. Cardiac research aimed at improving patient care is therefore multifaceted, and there is a push to keep producing more complete models to not only describe cardiac function, but to make predictions to aid in intervention. Cardiac mechanics and the finite element method have been a part of this push, and this work aims to contribute by implementing a physiologically motivated active contraction model.

Finite element (FE) modeling has been used increasingly for cardiac research, typically for simulations of the left ventricle (LV) during the cardiac cycle (Guccione & McCulloch, 1993; Guccione, Waldman, & McCulloch, 1993). Some of these models are phenomenological and are able to show reasonable agreement between FE predicted strains and experimental data (Guccione et al., 1993; Hunter, McCulloch, & ter Keurs, 1998), while others incorporate cellular level contraction models (Campbell, Janssen, & Campbell, 2018; Rice, Wang, Bers, & de Tombe, 2008) into LV models to reproduce organ level phenomena such as pressure-volume loops (PV-loops), linear end-systolic pressure-volume relationships (ESPVR), etc. (Shavik, Wall, Sundnes, Burkhoff, & Lee, 2017; Xiaoyan Zhang, Liu, Campbell, & Wenk, 2018). These descriptions of ventricular behavior are used in comparison between healthy and diseased hearts. Models that can bridge the gap between physiological mechanisms and clinically relevant characteristics may better translate to patient care.

A. V. Hill's early work defining properties of muscle mechanics (Hill, 1938) were essential in the development of later contraction models. Huxley followed up on this work and

proposed the sliding filament theory in 1953. Since, there have been multiple models that have expanded on the Huxley two-state model (Trayanova & Rice, 2011) (A. F. Huxley, 1957). These various models have been shown to capture certain experimentally observed properties of myocytes such as thick and thin filament cooperativity, force-velocity relationships, tension-recovery, etc. (Campbell et al., 2018; Land & Niederer, 2015; Rice et al., 2008; Schneider, Shimayoshi, Amano, & Matsuda, 2006). Through collaboration with Dr. Ken Campbell, the MyoSim model of contraction is implemented.

The work presented here is focused on the implementation of a physiologically motivated active contraction model into two finite element method frameworks: one existing explicit framework that exists as a custom material coded in the commercial software LS-DYNA, and a more generic form of the cell contraction model in a newly developed implicit finite element framework coded in the open-source software FEniCS. It also presents applications of these frameworks, highlighting the usefulness in investigating the interplay between cell level mechanisms and organ level function, and discusses preliminary work to set up investigations into cardiac growth and remodeling.

CHAPTER 2: CONSTITUTIVE EQUATIONS

As previously discussed, striated tissue is comprised of a highly organized multi-scale system. To model this system, constitutive equations have been developed to describe both the passive stress response of the tissue and the active stress generation. To discuss these equations, first consider a representative selection of contractile tissue (Figure 2.1):
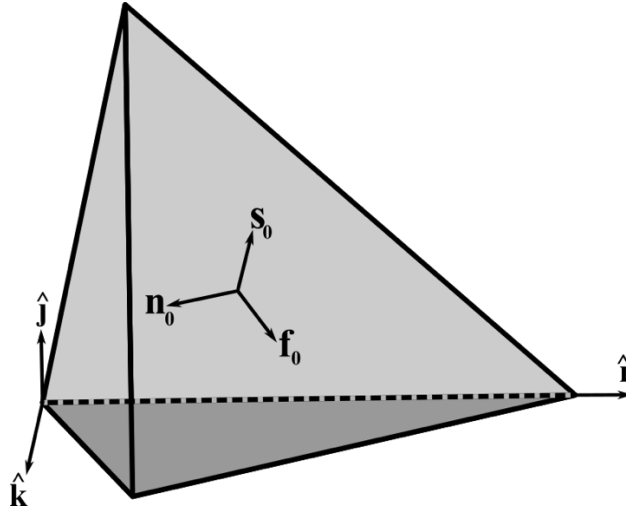
Figure 2.1: Representative Element. A representative selection of contractile tissue. A local coordinate system ($\mathbf{f_0}, \mathbf{s_0}, \mathbf{n_0}$) is defined to describe the prevailing fiber, sheet, and sheet normal directions respectively. It should be noted that the local coordinate system in general is different than the cartesian coordinate system ($\hat{\imath}, \hat{\jmath}, \hat{k}$) used as the basis for the reference and current configurations.

In accordance with the structure of contractile tissue, a local coordinate system is defined based on the prevailing fiber, sheet, and sheet-normal directions. This local coordinate system is orthogonal and defines the basis used to formulate the constitutive equations. Ultimately, the goal is to define the stress tensor S as a function of the deformation defined by the deformation gradient F and activation state of the tissue. To do this, the total stress S is additively decomposed into an active component (S_a) and a passive component (S_p):

$$S = S_a + S_p$$

This stress is used in the definition of the weak form to be discussed in chapter three.

2.1: Passive Tissue Response

The tissue is modeled as either nearly or completely incompressible, hyperelastic, and transversely isotropic with the response to deformation in the $\boldsymbol{f}_0$ direction differing from that in the $\boldsymbol{s_0}$ and $\boldsymbol{n_0}$ directions. The passive response of tissue is decomposed into a volumetric component and isochoric component. The isochoric component is further decomposed into two parts: the response of the myofiber and the response of the remaining bulk tissue consisting of the extra cellular matrix and connective tissue. As a hyperelastic material, a strain energy function was used for each response and the total passive stress obtained by differentiating their sum:

$$
\begin{aligned}
\boldsymbol{S_p} &= \boldsymbol{S_{vol}} + \boldsymbol{S_{bulk}} + \boldsymbol{S_{myofiber}} \\
&= \frac{\partial W_{vol}}{\partial \boldsymbol{E}} + \frac{\partial W_{bulk}}{\partial \boldsymbol{E}} + \frac{\partial W_{myofiber}}{\partial \boldsymbol{E}}
\end{aligned}
$$

where

$$
W_{vol} = \begin{cases} -p(J-1) & implicit \\ \dfrac{K}{2}(J-1)^2 & explicit \end{cases}
$$

$$
W_{bulk} = \frac{C}{2}\left(e^{\left(b_f E_{ff}^2 + b_t (E_{ss}^2 + E_{nn}^2 + E_{sn}^2) + b_{fs}\left(E_{fs}^2 + E_{sf}^2 + E_{fn}^2 + E_{nf}^2\right)\right)} - 1 \right)
$$

$$
W_{myofiber} = \begin{cases} C_2\left[e^{C_3(\alpha-1)^2} - 1\right] & \alpha > 1 \\ 0 & \alpha \leq 1 \end{cases}
$$

W_{vol} enforces incompressibility either via a Lagrange multiplier approach to enforce $J = \det(\mathbf{F}) = 1$ (used in the implicit formulation) or via a penalty method where K is the bulk modulus (used in the explicit formulation). W_{bulk} is the transversely isotropic strain energy function implemented by Guccione (Guccione et al., 1993), and E_{ff}, E_{nn}, E_{ss} represent the Green-Lagrangian fiber strain, sheet-normal strain, and sheet strain respectively, and the other terms represent shear strains. The degree of transverse isotropy is governed by the parameters b_f, b_t, and b_{fs} and C is an isotropic scaling factor. $W_{myofiber}$ is an exponential strain energy function implemented in (Xi, Kassab, & Lee, 2019) where C_2, C_3 are material constants, α is the myofiber stretch calculated as

$$\alpha = \sqrt{f_0 \cdot C \cdot f_0}$$

and $C = F^T F$ is the right Cauchy-Green deformation tensor. It is assumed that the myofiber does not bear any compressive load.

2.2: Active Stress Generation (MyoSim)

Active stress is calculated at each integration point within a finite element, representing the behavior of the half-sarcomeres within the tissue. To do so, the MyoSim (Campbell, 2014) model has been incorporated in the finite element framework. MyoSim extends Huxley's (A. F. Huxley, 1957) cross-bridge distribution technique. This technique is essentially a population model representing the relative population of myosin heads on the thick filament that inhabit one of a number of states (depending on the kinetic scheme being considered). Mathematical descriptions of the transitions between these states produce a system of ordinary differential equations that once solved, results in a population of cross-bridges that are modeled as linearly elastic that produce force.

MyoSim extends this approach by incorporating activation of the actin (thin) filament in the presence of intracellular calcium and dynamic coupling of the thick and thin filaments (Campbell, 2014). Since its introduction, MyoSim has been used to investigate phenomena such as cooperativity, the mechanisms involved in relaxation (Campbell, 2016; Chung, Hoopes, & Campbell, 2017), and potential mechanisms involving the recently discovered super-relaxed state of myosin that contribute to length-dependent activation (Campbell et al., 2018). Base assumptions that have been used in the model kinetic schemes will be explained in detail.

Base Assumptions

MyoSim is flexible in that different kinetic schemes can be set by the researcher, but all simulations have some common assumptions:

- While the intracellular calcium concentration ($[Ca^{2+}]$) influences thin filament activation, the reverse is not true

- Binding sites on the thin filament exist in an off state (N_{OFF}), on and unbound state ($N_{UNBOUND}$), or on and bound state (N_{BOUND})
- Myosin heads can only attach to binding sites in the $N_{UNBOUND}$ state
- Cross-bridge links are assumed to be linearly elastic (and can sustain "negative force" interpreted as resistance to shortening)
- Binding sites that are activated cannot become inactive while a myosin head is attached, i.e. there is no direct transition from N_{BOUND} to N_{OFF}
- Only a fraction of a half-sarcomere's length change is transmitted to cross-bridges, accounting for filament compliance (H. E. Huxley, Stewart, Sosa, & Irving, 1994; Tajima, Makino, Hanyuu, Wakabayashi, & Amemiya, 1994)
- The maximum number of binding sites that can potentially form cross-bridges at a given time is set by $N_{OVERLAP}$:

$$N_{OVERLAP} = \begin{cases} 0 & if \ l_{overlap} \leq 0 \\ \dfrac{l_{overlap}}{l_{max \ overlap}} & if \ 0 < l_{overlap} < l_{max \ overlap} \\ 1 & if \ l_{max \, overlap} \leq l_{overlap} \end{cases}$$

where

$$l_{overlap} = l_{thin} + l_{thick} - l_{sarcomere}$$
$$l_{max \ overlap} = l_{thick} - l_{bare}$$

l_{thin}, l_{thick}, $l_{sarcomere}$, and l_{bare} are the lengths of the thin filament, thick filament, sarcomere, and thick filament bare zone, respectively. In the case that $l_{sarcomere} < l_{thin}$

$$N_{overlap} = 1 - l_{falloff}(l_{thin} - l_{sarcomere})$$

where $l_{falloff}$ is a parameter describing the fraction of binding sites that are removed from the overlap in the model. The inclusion of $N_{overlap}$ gives active stress dependence on muscle length.

Kinetic Schemes

Two kinetic schemes will be described. First, a three state scheme including force-dependent recruitment from the myosin super-relaxed state was used to investigate how this recruitment impacts LV function (Mann, Lee, Campbell, & Wenk, 2020). Second, a four state scheme including a pre-power stroke attached state was used in a study investigating disarray effects on contraction. It should be noted that a simple two state kinetic scheme was previously used to successfully drive active contraction in a finite element model (Xiaoyan Zhang et al., 2018).

Three-State Kinetic Scheme With Super-Relaxed State:

Binding sites are assumed to inhabit one of three states: N_{OFF}, $N_{UNBOUND}$, or N_{BOUND} as describe in the base assumptions. Myosin heads are assumed to inhabit a super-relaxed state (M_{SRX}), disordered-relaxed state (M_{DRX}), or force-generating state ($M_{FG}(x)$). The force-generating state is a function of the location of the cross-bridge linkage, with $x = 0$ representing a cross-bridge formed at a binding site directly opposite the myosin head. The x domain is discretized into n intervals over a specified working cross-bridge range. In this scheme, only heads in the $M_{FG}(x)$ state produce force. A schematic of this approach can be seen in Figure 2.2:
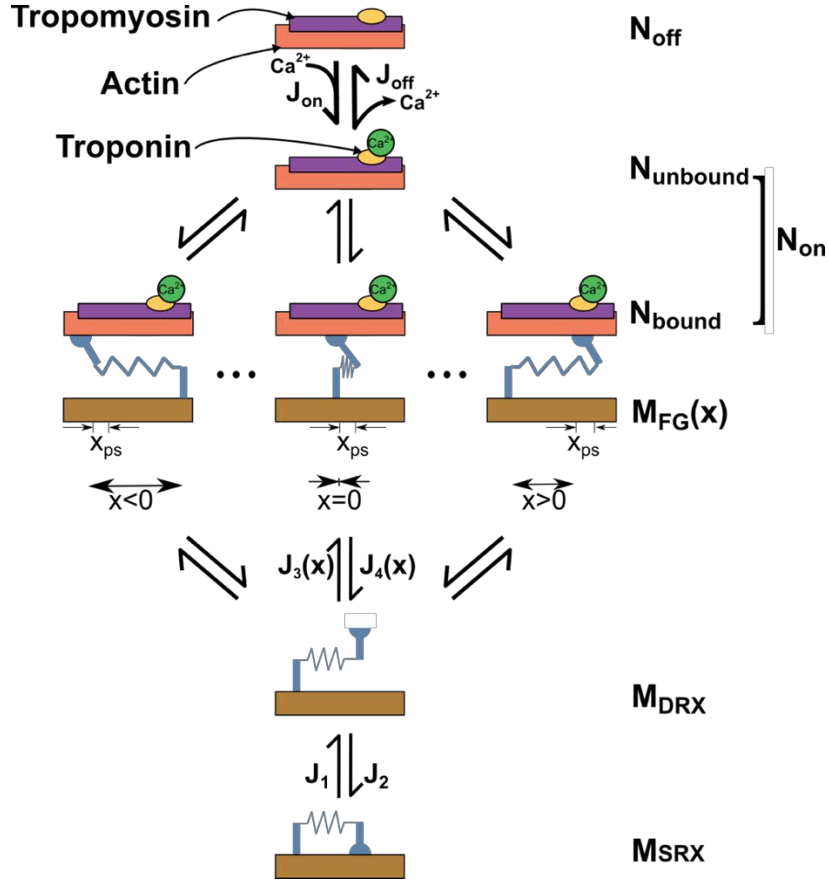
Figure 2.2: 3 State Kinetic Scheme. Schematic of three-state contraction scheme with the super-relaxed myosin state. Adapted from (Campbell, Chrisman, & Campbell, 2020).

Thin filament transitions are given by

$$\frac{dN_{OFF}}{dt} = -J_{ON} + J_{OFF}$$

$$\frac{dN_{ON}}{dt} = -J_{OFF} + J_{ON}$$

where J_{ON} and J_{OFF} are the fluxes through the N_{ON} and N_{OFF} states, respectively, defined as

$$J_{ON} = k_{ON}[Ca^{2+}](N_{OVERLAP} - N_{ON})\left(1 + k_{COOP}\left(\frac{N_{ON}}{N_{OVERLAP}}\right)\right)$$

$$J_{OFF} = k_{OFF}(N_{ON} - N_{BOUND})\left(1 + k_{COOP}\left(\frac{N_{OVERLAP} - N_{ON}}{N_{OVERLAP}}\right)\right)$$

and k_{ON}, k_{OFF}, and k_{COOP} are rate constants. In the event that $N_{OVERLAP} \leq N_{ON}$, the $(N_{OVERLAP} - N_{ON})$ term is set to zero so that no more binding sites on the thin filaments can activate, and there is no cooperative detachment effect from off binding sites. These ODEs describe a population that activates in the presence of calcium, and binding sites that turn on/off influence others to do the same.

The thick filament transitions are given by

$$\frac{dM_{SRX}}{dt} = -J_1 + J_2$$

$$\frac{dM_{DRX}}{dt} = \left(J_1 + \sum_{i=1}^{n} J_{4,x_i}\right) - \left(J_2 + \sum_{i=1}^{n} J_{3,x_i}\right)$$

$$\frac{dM_{FG,i}}{dt} = J_{3,x_i} - J_{4,x_i}$$

where $J_1 \to J_4$ are the fluxes through the myosin states, with i representing the ith interval over the x domain, defined as

$$J_1 = k_1\left(1 + k_{FORCE}(F_{P,fiber} + T)\right)M_{SRX}$$

$$J_2 = k_2 M_{DRX}$$

$$J_{3,x_i} = k_3 e^{\frac{-k_{cb}x_i^2}{2k_B T_k}} M_{DRX}(N_{ON} - N_{BOUND})$$

$$J_{4,x_i} = (k_{4,0} + k_{4,1}x_i^4)M_{FG,x_i}$$

In the above, $k_1 \to k_{4,1}$ are rate constants, k_{cb} is the stiffness of a cross-bridge, k_B is Boltzmann's constant, T_k is the temperature in Kelvin, T is the current active stress in the half-sarcomere, and $F_{P,fiber}$ is the passive stress experienced by the half-sarcomere:

$$F_{P,fiber} = \boldsymbol{f_0} \cdot \boldsymbol{S_{myofiber}} \cdot \boldsymbol{f_0}$$

Note that J_1 includes both active and passive stress, thus a non-activated, stretched sarcomere will more quickly recruit myosin heads from the super-relaxed state. Note also that the thick and thin filament populations are coupled due to the inclusion of the (N_{ON} − N_{BOUND}) term in the flux through the M_{DRX} state. Together, these ODEs describe a population of myosin heads that get recruited from the super-relaxed state and form cross-bridges. The formation of cross-bridges is highest on binding sites directly opposed to the myosin head, and detachment is highest the farther the cross-bridge is strained from $x =$ 0 due to changes in half-sarcomere length. This three-state MyoSim scheme was first introduced to investigate the existence of a force-dependent recruitment from the super-relaxed state. Simulations suggest that this force-dependent recruitment contributes to length-dependent activation and the Frank-Starling mechanism (Campbell et al., 2018).

Four-State Kinetic Scheme:

The four state scheme contains all of the states from the three state kinetic scheme but adds a weakly bound, pre-power stroke state (Figure 2.3):
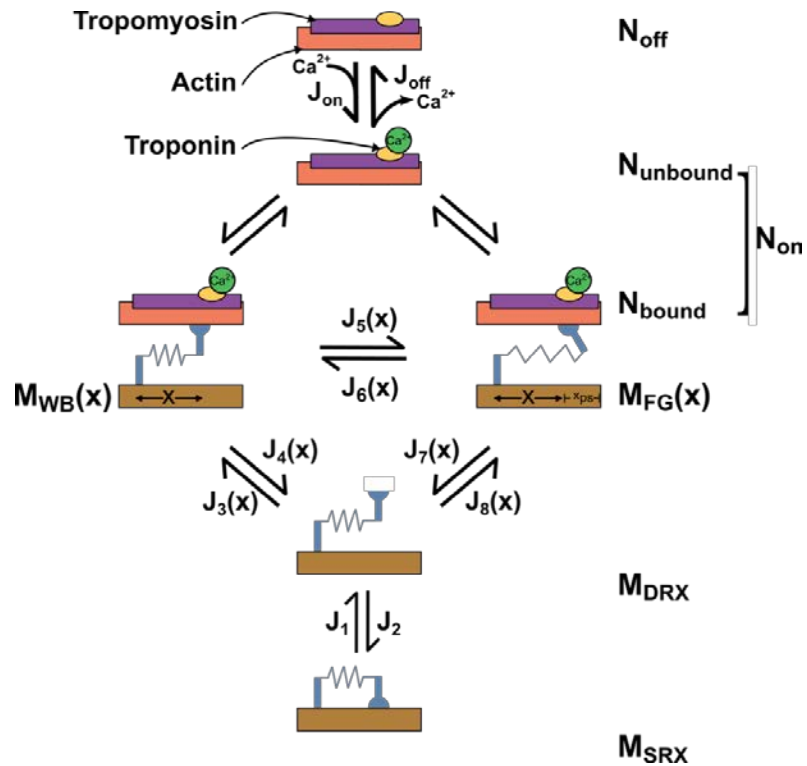
Figure 2.3: 4 State Kinetic Scheme. Schematic of the four-state kinetic scheme including the super-relaxed myosin state and weakly bound pre-power stroke state.

The weakly bound state is an attached state similar to $M_{FG}(x)$, however the power stroke distance is set to zero. This results in a state that only contributes active force when its population is perturbed due to length change, producing a viscous effect. To better illustrate this, consider the representative populations in $M_{FG}(x)$ and $M_{WB}(x)$ shown in Figure 2.4.
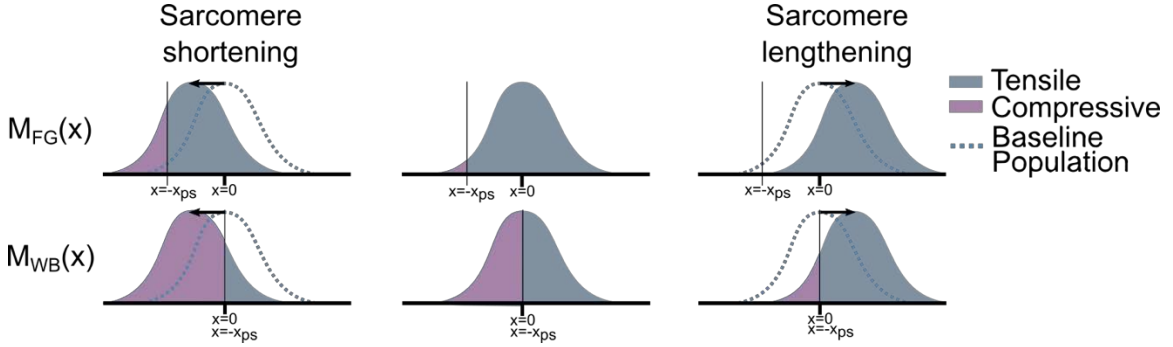
Figure 2.4: Force Generating Populations. Representative populations for the force generating state (top middle) and weakly bound state (bottom middle) as a function of distance from the myosin head. Cross-bridges to the right of the line x = -x_{ps} produce a tensile force while those to the left produce compressive. Sarcomere lengthening shifts the populations to the right, increasing the tensile force produced, and conversely shortening decreases the net tensile force. In the case of applied loading, the net force produced is equal to the load applied. Shortening velocity is dictated by the displacement needed to balance loading, and is maximum for unloaded shortening.

Cross-bridge populations are shifted to the right in the x-domain during half-sarcomere re-lengthening, and to the left for half-sarcomere shortening. Cross-bridges that are attached to the right of $(x - x_{ps})$ produce a tensile active stress, otherwise they detract from the overall stress generated. In the case of an applied load P, a sarcomere will undergo a length change to achieve force balance. In the case of the weakly bound population with no power stroke distance, stress is produced only during length changes, which has implications for the shortening velocity achieved and work done during shortening.

The thick filament transitions for this scheme are described by

$$\frac{dM_{SRX}}{dt} = -J_1 + J_2$$

$$\frac{dM_{DRX}}{dt} = J_1 + \left(\sum_{i=1}^{n} J_{4,x_i} + J_{7,x_i}\right) - J_2 - \left(\sum_{i=1}^{n} J_{3,x_i} + J_{8,x_i}\right)$$

$$\frac{dM_{WB,i}}{dt} = \left(\sum_{i=1}^{n} J_{3,x_i} + J_{6,x_i}\right) - \left(\sum_{i=1}^{n} J_{4,x_i} + J_{5,x_i}\right)$$

$$\frac{dM_{FG,i}}{dt} = \left(\sum_{i=1}^{n} J_{8,x_i} + J_{5,x_i}\right) - \left(\sum_{i=1}^{n} J_{6,x_i} + J_{7,x_i}\right)$$

with $J_1 \rightarrow J_4$ as previously defined, and $J_5 \rightarrow J_8$ defined as

$$J_{5,x_i} = k_{5,0}\left(1 + e^{k_{5,1}\left(x_i + \frac{x_{ps}}{2}\right)}\right)^{-1}$$

$$J_{6,x_i} = k_6$$

$$J_{7,x_i} = k_{7,0} + (k_{7,1}x_i^4)$$

$$J_{8,x_i} = k_8$$

Finally, active stress can be calculated using the relative populations in all attached states as:

$$T = \sum_{\gamma \in attached} \int_{-\infty}^{\infty} \rho_m k_{cb} M_\gamma(x)(x + x_{ps,\gamma})dx$$

where ρ_m is the theoretical number of myosin heads in a half-sarcomere of cross-sectional area of 1 m^2, x is the distance of the cross-bridge link from $x = 0$, and $x_{ps,\gamma}$ is the power stroke distance for attached state γ. The active stress tensor is then calculated as

$$\boldsymbol{S_a} = [T(\boldsymbol{f}_0 \otimes \boldsymbol{f}_0) + \mu T(\boldsymbol{s}_0 \otimes \boldsymbol{s}_0) + \mu T(\boldsymbol{n}_0 \otimes \boldsymbol{n}_0)]$$

The active stress from MyoSim is assigned along the referential fiber direction. Due to sarcomeric branching and cross-linking of connective tissue, a fraction of the active stress can be transmitted in the sheet and sheet-normal directions as dictated by the scalar value μ.

CHAPTER 3: IMPLEMENTATION

The constitutive equations from chapter two have been implemented in two separate finite element frameworks: the explicit nonlinear FE solver LS-DYNA (Livermore Software Technology Corporation, Livermore, CA, USA) and the open source partial differential equation solver FEniCS (Logg, 2012).

3.1: Explicit FEM and LS-DYNA

LS-DYNA uses an explicit time integration scheme, specifically the central difference method. This software allows custom materials to be modeled by coding a user defined material subroutine. It is within this subroutine that the passive constitutive equation and three-state MyoSim kinetic scheme are implemented. Near incompressibility in this framework is enforced via a penalty method as described in chapter two. A simplified flowchart of the user defined subroutine implemented can be seen in Figure 3.1:
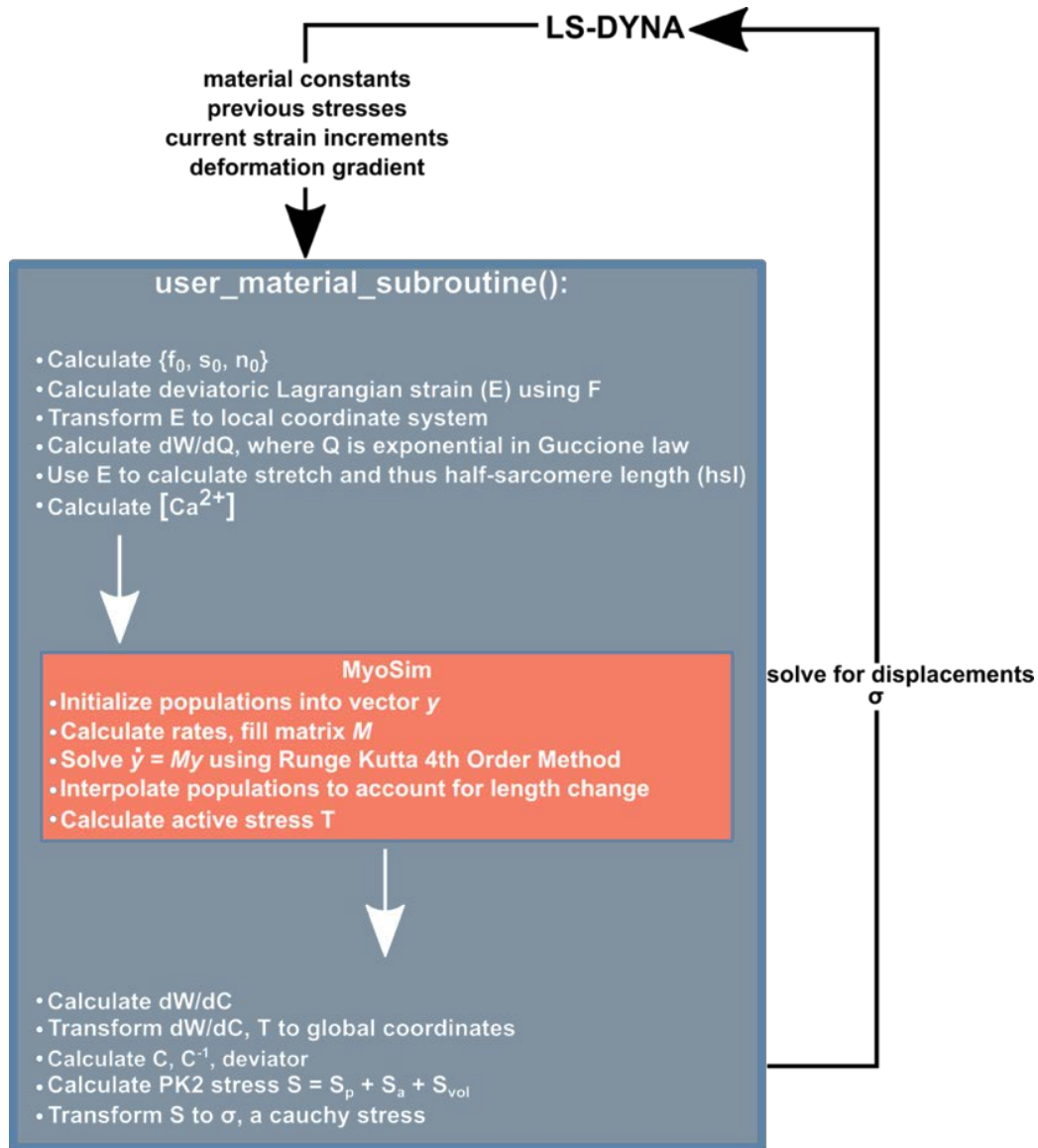
Figure 3.1: Explicit Subroutine. Flowchart showing the relevant quantities calculated by the user defined subroutine and the flow of information during one time step.

Meshes were generated using TrueGrid software (TrueGrid; XYZ Scientific, Inc., Livermore, CA, USA) and cardiovascular magnetic resonance imaging (CMR). The mesh consisted of linear hexahedral elements with one integration point to under-integrate in order to avoid shear locking. The user defined subroutine was executed at each integration point. In left ventricular simulations, the cavity volume was used as a boundary condition and controlled by specifying a volumetric flow rate into and out of the ventricle, estimated using CMR. A two-state MyoSim kinetic scheme was previously implemented (Xiaoyan Zhang et al., 2018) and showed that by optimizing contraction parameters to produce a

pressure profile similar to that experimentally measured, strains calculated from DENSE CMR could be reproduced. This framework with the three-state scheme was used to investigate how the force-dependent recruitment affects organ level function (Mann et al., 2020).

3.2: Implicit FEM in FEniCS (MyoFE)

Recent work has shifted from using LS-DYNA to FEniCS, an open source partial differential equation solver. FEniCS has a Python interface and uses UFL (unified form language) to specify weak forms and allows for flexibility and complete control. The new framework with MyoSim contraction schemes implemented is called MyoFE and is available through Github (https://github.com/MMoTH/FEniCS-Myosim).

This framework uses quadratic tetrahedral finite elements to solve for the displacement, and linear tetrahedral elements for the hydrostatic pressure. Total incompressibility is assumed, and a Lagrange multiplier approach is used. Similar to the explicit framework, cell contraction schemes are solved at each integration point. In this framework, a "quadrature" element of degree 2 is used. Note, integration point coordinates are not in general equal to the element node points). In an attempt to provide flexibility and ease of scaling, this framework is modular in nature. Though MyoFE can be used to solve problems over different geometries and boundary conditions, the general structure for each simulation is preserved and can be seen in Figure 3.2.

This framework is coded in a modular way in an attempt to provide flexibility and aid in future scaling. Specifics regarding problem weak forms and boundary conditions will be discussed in detail in later chapters defining specific studies. Advantages to using this framework include: the unconditional stability that comes with an implicit integration scheme, allowing for larger time steps to be taken. Complete developmental control, for example the ability to implement arbitrary circulatory models as boundary conditions which could not be done in LS-DYNA.

MyoFE

Main File   Call to Module   MyoSim Package

- **Load in all parameters from .json instruction file**

- **Optional: Load in previous solution**

IMPORT_MESH()

- **Initialize dolfin expressions**

- **Initialize finite elements**

- **Define function spaces using mesh and finite elements**

INITIALIZE_DOLFIN_FUNCTIONS()

- **Create solution function, test and trial functions**

ASSIGN_INITIAL_HSL()

ASSIGN_LOCAL_COORDINATE_SYSTEM()

ASSIGN_HETEROGENEOUS_PARAMS()

- **Create growth tensors**

FORMS()

SET_BOUNDARY_CONDITIONS()

- **Define weak form**

- **If ventricle simulation, perform initial diastolic loading**

- **Initialize half-sarcomere object**

- **Initialize cell ion object**

- **If ventricle simulation, initialize circulatory model**

TIME LOOP

UPDATE_CIRC_COMPARTMENTS()

CALCULATE_ION_CONCENTRATIONS()

MYOSIM()

- **Solve weak form**

- **Update relevant quantities (hsl, stresses, etc.)**

UPDATE_LOCAL_COORDINATE_SYSTEM()

UPDATE_BOUNDARY_CONDITIONS()

GROW_MESH()

SAVE_SOLUTION()

Figure 3.2: MyoFE Algorithm. High level summary of the MyoFE code. Elements that remain consistent between different types of simulations remain in the main file (blue background) while calls to modules appropriately handle different cases (yellow background).

CHAPTER 4: MYOSIN FORCE-DEPENDENT RECRUITMENT INCREASES END-SYSTOLIC PRESSURE-VOLUME RELATIONSHIP

This chapter is content reproduced from *Mann, Lee, Campbell & Wenk, Force-Dependent Recruitment From Myosin OFF-State Increases End-Systolic Pressure-Volume Relationship in Left Ventricle. Biomechanics and Modeling in Mechanobiology: 2020.*

4.1: Background

Finite element (FE) modeling has been used increasingly for cardiac research, typically for simulations of the left ventricle (LV) during the cardiac cycle (Guccione & McCulloch, 1993; Guccione et al., 1993). Some of these models are phenomenological and are able to show reasonable agreement between FE predicted strains and experimental data (Guccione et al., 1993; Hunter et al., 1998), while others incorporate cellular level contraction models (Campbell et al., 2018; Rice et al., 2008) into LV models to reproduce organ level phenomena such as pressure-volume loops (PV-loops), linear end-systolic pressure-volume relationships (ESPVR), etc. (Shavik et al., 2017; Xiaoyan Zhang et al., 2018). These descriptions of ventricular behavior are used in comparison between healthy and diseased hearts. Specifically, the ESPVR is used in research settings as a measure of contractility. Efforts have been made to find ways to use ESPVR or estimations of it in the clinic (Burkhoff, Mirsky, & Suga, 2005; Shoucri & Kohar, 2012). Models that can bridge the gap between physiological mechanisms and clinically relevant characteristics may better translate to patient care.

There are multiple models of contraction (Trayanova & Rice, 2011) that have expanded upon the Huxley two-state model (A. F. Huxley, 1957). These models have been shown to capture certain experimentally observed properties of myocytes such as thick and thin filament cooperativity, force-velocity relationships, tension-recovery, etc. (Campbell et al., 2018; Rice et al., 2008; Schneider et al., 2006). Length-dependent activation in muscles is well documented experimentally, but the underlying mechanisms remain unclear. One of the recent hypotheses is that structural re-arrangement of thick filaments contributes. Specifically, it is hypothesized that length-dependent activation reflects recruitment of

17

myosin heads from a super-relaxed state (which cannot interact with actin) to a disordered-relaxed state (which can interact with actin) (Ait-Mou et al., 2016; Kampourakis, Sun, & Irving, 2016). This hypothesis is supported by simulations which reproduce length-dependent activation measured in isolated myocardium when the rate of the super-relaxed to disordered-relaxed transition increases linearly with force (Campbell et al., 2018).

The current study implements the three-state contraction model (myosin super-relaxed (SRX) state, myosin disordered-relaxed (DRX)-state, and myosin force-generating state (FG)) from that work into an existing nonlinear 3D FE code to model healthy Sprague-Dawley rat LVs. As the myosin force-dependent transition is dependent on total stress within the sarcomere, the passive response of the tissue is decomposed into that of the myofiber and the remaining bulk material (i.e., collagen, elastin, gel-like cells, interstitial fluid, etc), moving towards a more structurally based passive constitutive law. This method was validated using the animal-specific FE models, which were fit to experimentally measured LV pressures and then compared to experimentally measured end-systolic strain. It is shown that the model predictions are in good agreement with experimental measurements, and that length-dependent activation is captured both at multiple scales as seen in physiologically realistic force-pCa curves and ESPVR values calculated from simulations. Furthermore, it is shown that when the FE models are optimized using a previously developed two-state cellular contraction model ("two-state model") where the myosin SRX-state is omitted (Xiaoyan Zhang et al., 2018), the ESPVR values calculated are less than those calculated from the three-state implementation, suggesting that transitions to and from the myosin SRX-state contribute to the Frank-Starling mechanism seen at the organ level.

4.2: Methods

Details of the experiments have been published (X. Zhang et al., 2017). Briefly, 3D displacement encoding with stimulated echoes cardiovascular magnetic resonance (DENSE CMR) imaging was conducted (7T Bruker ClinScan system, Bruker, Ettlingen, Germany) on 5 female Sprague-Dawley rats. These images were used to create contours of the LV wall for FE mesh generation, and then calculations were performed using DENSE

analysis (Spottiswoode et al., 2007) to assess end-systolic strains. This was followed by LV pressure measurements using a pressure transducer (SPR-903, Millar Instruments, Houston, TX, USA). All animal procedures were approved by the Institutional Animal Care and Use Committee at the University of Kentucky and were in agreement with the guidelines by the National Institutes of Health for the care and use of laboratory animals (NIH Publication 85–23, revised 1996). All values are reported as mean ± standard deviation.

For each of the animals, an LV FE model was created based on geometric surfaces generated from the CMR data. The reference configuration of the LV was defined to be at early diastole. The mesh was created using 8-node hexahedral brick elements, and the myocardium was split into three layers: epicardium, mid-myocardium, and endocardium (X. Zhang, Haynes, Campbell, & Wenk, 2015). Each layer was assigned unique reference sarcomere lengths of 1910 nm, 1850 nm, and 1780 nm from epicardium to endocardiuim, respectively (Guccione et al., 1993). Helical fiber angles (f_0) were also assigned to each layer as -60°, 0°, and +60°, relative to the circumferential direction, in the epicardium, mid-myocardium, and endocardium, respectively (Figure 4.1). It should be noted that in the current study, the sheet angle was set to 0°. Finally, endocardial contours were drawn at multiple time points on each CMR image during the filling phase and ejection phase. This contour data was then used to estimate the LV cavity volume as a function of time during the entire cardiac cycle and was implemented in the simulation as a boundary condition specifying the volumetric flowrate (dV/dt) into and out of the LV. The explicit LS-DYNA formulation discussed in chapter two was used for this study. Note that this means near-incompressibility was enforced. Also, the three state MyoSim kinetic scheme was employed (Figure 2.2).
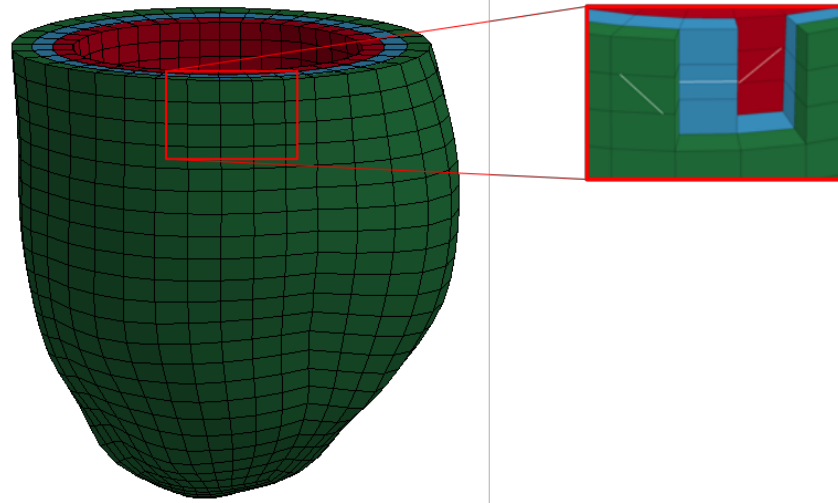
Figure 4.1: Representative mesh and helical fiber angles. Representative left ventricular finite element mesh (TrueGrid; XYZ Scientific, Inc., Livermore, CA, USA) generated from cardiac magnetic resonance imaging. The LV is partitioned into three parts; epicardium (green), mid-myocardium (blue) and endocardium (red). The highlighted section is displaying assigned helical fiber angles for each section (-60° epicardium, 0° mid-myocardium, +60° endocardium). Material from: Mann, Lee, Campbell & Wenk, Force-Dependent Recruitment From Myosin OFF-State Increases End-Systolic Pressure-Volume Relationship in Left Ventricle, Biomechanics and Modeling in Mechanobiology, published 2020, Springer-Verlag GmbH Germany, part of Springer Nature.

Each simulation was performed for the time-course of one cardiac cycle, beginning at end-systole from the reference configuration. Boundary conditions include (i) constraining nodes at the base of the ventricle longitudinally (coincident with the z-direction), (ii) allowing nodes at the base to expand radially, and (iii) fixing ventricular volume at a value calculated at each time step from the specified flowrate boundary condition (Figure 4.2). Additionally, an intracellular calcium transient was specified, which was adapted from experimental measurements (Laurita & Singal, 2001) and independent of the cross-bridge kinetics (Figure 4.2). The peak value of calcium was based on (Campbell et al., 2018). At each time step, the change in cavity volume causes the wall to deform, which induces stretch along the myofiber direction, and thus changes the sarcomere length. This change in sarcomere length, along with the passive stress in the myofiber, active stress from the previous time step, and calcium concentration ($[Ca^{2+}]$) are used by the cellular contraction model to calculate active stress produced by a sarcomere. This active stress is then scaled up proportionally by the density of myosin heads in a cardiac sarcomere. The total stress state in the LV wall, which is the sum of the passive and active stress, is then balanced by

the calculated intraventricular pressure. Note, the cell contraction model is solved at each time step, even during diastole.
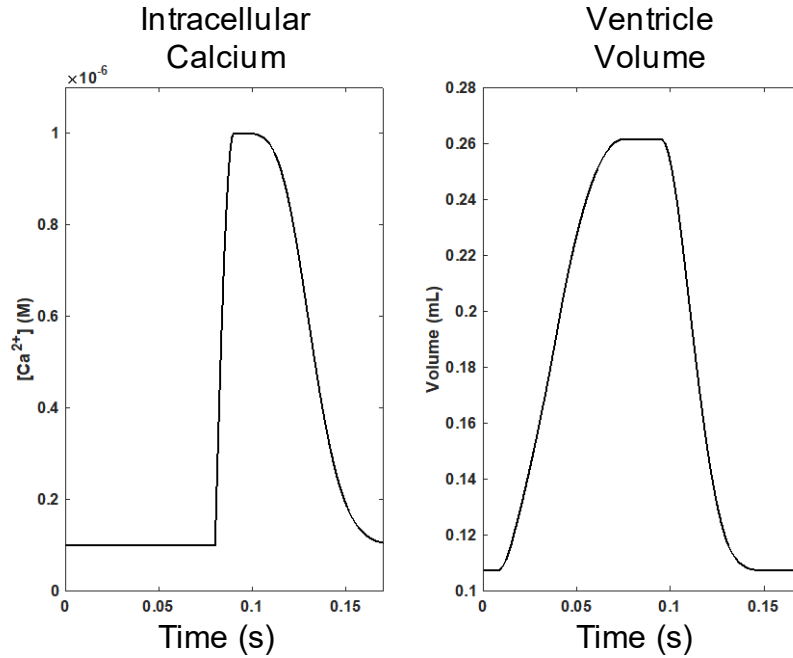
Figure 4.2: Calcium and Cavity Volume. Representative intracellular calcium transient (a) and ventricular volume (b) used to drive simulations. Material from: Mann, Lee, Campbell & Wenk, Force-Dependent Recruitment From Myosin OFF-State Increases End-Systolic Pressure-Volume Relationship in Left Ventricle, Biomechanics and Modeling in Mechanobiology, published 2020, Springer-Verlag GmbH Germany, part of Springer Nature.

Passive parameters for the strain energy functions (C, C_2 and C_3 fix formatting) were chosen such that the end-diastolic pressure from the models matched experimentally measured end-diastolic pressures, and such that the bulk material stress was approximately twice that of the myofibers at end-diastole (Xi et al., 2019). Values chosen were C = 0.266 ± .087 kPa, C_2 = 0.172 ± .063 kPa, and C_3 = 7.6 ± 4. Simulations were performed to end-diastole iteratively to select the final values of these parameters.

Parameters for the embedded cellular contraction model were numerically optimized using LS-OPT (Livermore Software Technology Corporation, Livermore, CA) to minimize the difference between FE predicted ventricular pressures and experimentally obtained pressures. A hybrid approach using a combination of simulated annealing and the sequential response surface method was used as previously described (Xiaoyan Zhang et

al., 2018). Seven parameters were optimized, and pressures were compared at a minimum of seven time points during systole and relaxation. Ranges for these parameters were chosen to keep the transition rates within physiologically reasonable magnitudes. The parameters involved in the optimization can be found in Table 4.2.

Further validation of the models included comparing mid-ventricular end-systolic strains predicted by the models to experimentally measured strains from DENSE CMR. In order to provide multi-scaled validation, simulations were conducted using the final optimized parameters in single element FE models to mimic single cell experiments from the literature. These simulations included a cell developing maximum tension at saturating calcium, the generation of force-pCa curves to investigate length-dependent shifting of pCa_{50} values, and tension recovery simulations (ktr). Finally, vena cava occlusion was simulated in the LV FE models in order to generate a series of descending PV-loops (Figure 4.3) from which the ESPVR was calculated. In order to simulate a vena cava occlusion, the end-diastolic volume (EDV) was gradually reduced over a series of FE simulations. This was accomplished by scaling the volumetric flowrate that was used as a boundary condition to drive the simulation. Based on previous studies, the flowrate into the ventricle was reduced, while the flowrate out of the LV was adjusted to conserve the ejection fraction (Konstam & Abboud, 2017; Olah et al., 2015). This shifts the each PV loop down and to the left. In the current study, the end-diastolic volume was gradually reduced by 30%. This process was repeated in the LV model using a previous cellular contraction model that omitted the myosin-SRX state, i.e., the two-state model (Xiaoyan Zhang et al., 2018).
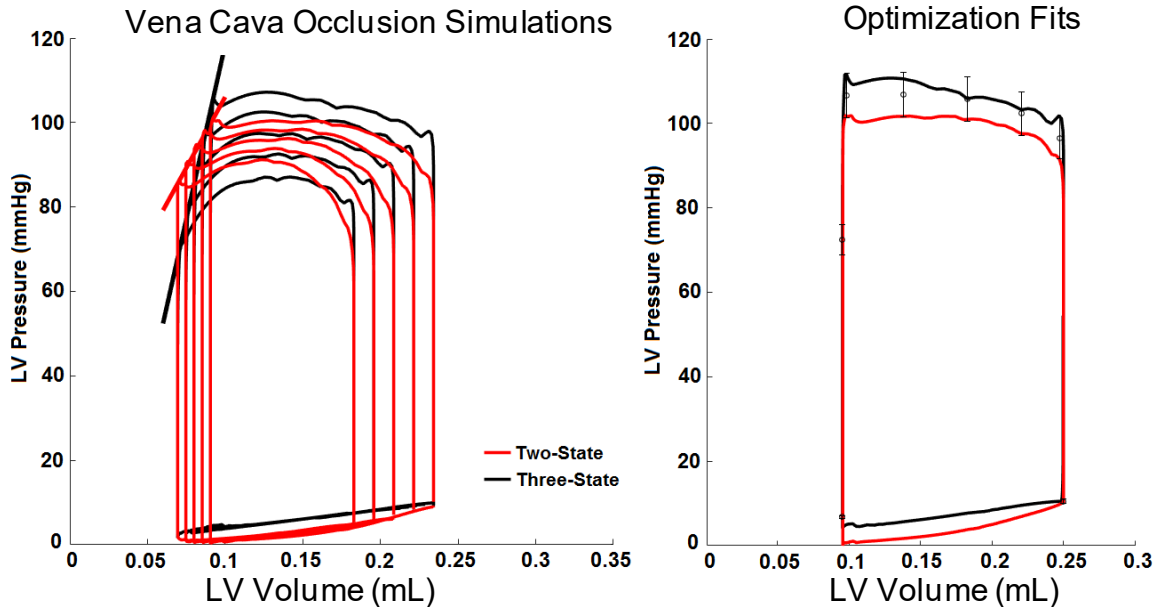
Figure 4.3: Representative PV Loops & Model Fit. Representative pressure-volume loops generated from simulating vena cava occlusion. The diagonal lines that are fitted to end-systole represent the end-systolic pressure volume relationship (ESPVR). (b) PV loops that were generated from optimization of the two-state and three-state models to the experimental data. Circular markers indicate experimentally measured values with range bars that represent ±5%. Material from: Mann, Lee, Campbell & Wenk, Force-Dependent Recruitment From Myosin OFF-State Increases End-Systolic Pressure-Volume Relationship in Left Ventricle, Biomechanics and Modeling in Mechanobiology, published 2020, Springer-Verlag GmbH Germany, part of Springer Nature.

4.3: Results

Organ Level Function

All five of the animal-specific FE models showed good agreement with the experimentally measured pressure values during the optimization procedure. An example of this can be seen in Figure 4. The overall fit to the pressure points during ejection and relaxation was within ±5% and the final optimized parameters are listed in Table 4.2. As noted before, each model was fit to the end-diastolic pressure and volume, so that the passive parameters C, C_2, and C_3 could be defined before the optimization. In order to further validate the models, and compare their performance to the previous two-state implementation (Xiaoyan Zhang et al., 2018), mid-ventricular end-systolic strain was calculated. Both the three-state and two-state models showed good agreement with 5 of the 6 CMR measured end-systolic strain components, i.e., no statistically significant difference was found (Table 4.1). With respect to the longitudinal strain, both implementations showed a statistically significant

difference from the CMR strain (-0.159±0.010 vs. -0.106±0.011 [CMR vs. 3-state] and -0.159±0.010 vs. -0.085±0.008 [CMR vs. 2-state], both $*p < 0.05$). However, the three-state model is also significantly different from the two-state model (-0.106±0.011 vs. -0.085±0.008, $\dagger p < 0.05$) and is closer to the CMR measured value.

Table 4.1: Strain Comparisons

	E_{cc}	E_{rr}	E_{ll}	E_{cr}	E_{cl}	E_{rl}
CMR	-0.200±0.022	0.553±0.075	-0.159±0.010	0.068±0.013	0.055±0.012	0.085±0.017
3 state	-0.189±0.011	0.522±0.061	-0.106±0.011*†	0.056±0.010	0.062±0.014	0.087±0.012
2 state	-0.185±0.010	0.510±0.056	-0.085±0.008*	0.058±0.014	0.064±0.011	0.091±0.013

*Table 3: End-systolic strain components averaged at the mid-LV in the mid-myocardial layer. Data are mean ± standard deviation; n = 5. Multiple comparisons between groups (i.e., experimental CMR, three-state model, two-state model) were performed using one-way ANOVA with post-hoc Bonferroni t-tests.*p < 0.05 for comparisons between model-predicted and experimentally measured strains. †p < 0.05 for comparisons between three-state model and two-state model.*

The simulated vena cava occlusion was conducted for each animal-specific LV FE model, using both the three-state and two-state contraction models. A representative set of PV loops, along with ESPVR slopes, are shown in Figure 4.3. The three-state ESPVR value with a force-dependent transition to the ON state is significantly higher than the two-state, where the SRX state is omitted ($p < 0.05$) (Figure 4.4). The average ESPVR from the three-state model was found to be 1380.89 ± 89.62 mmHg mL^{-1} and for the two-state model was 764.47 ± 148.01 mmHg mL^{-1}, which both fall near or within the physiologically realistic bounds of 1000-7000 mmHg mL^{-1} (Pacher, Nagayama, Mukhopadhyay, Batkai, & Kass, 2008).
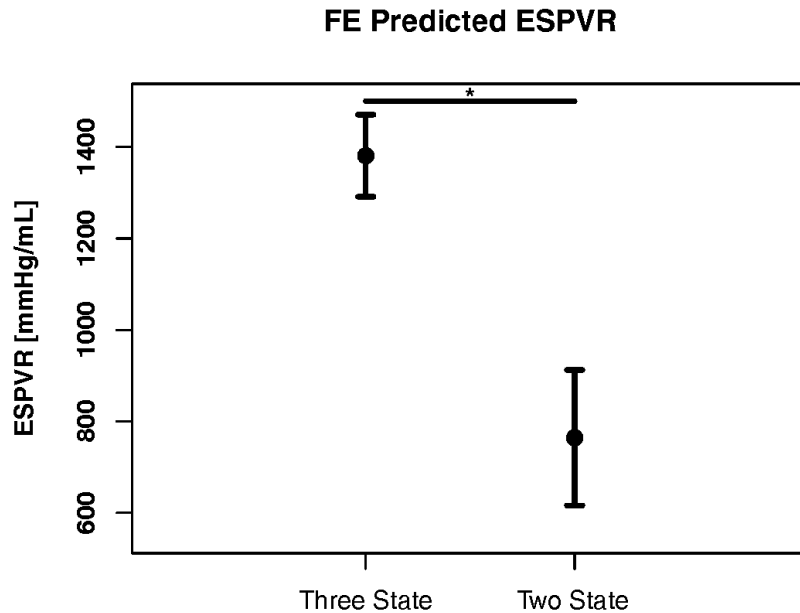
FE Predicted ESPVR

Figure 4.4: Model Predicted End-Systolic Pressure-Volume Relationships. Calculated ESPVR values for the three-state contraction model as compared to a two-state contraction model that omits the myosin OFF state; n=5. *p<0.05, unpaired Student's t-tests assuming equal variances. Material from: Mann, Lee, Campbell & Wenk, Force-Dependent Recruitment From Myosin OFF-State Increases End-Systolic Pressure-Volume Relationship in Left Ventricle, Biomechanics and Modeling in Mechanobiology, published 2020, Springer-Verlag GmbH Germany, part of Springer Nature.

Cellular Level Function

The results of the single element FE simulations for a sarcomere length of 2300 nm, which used the optimized parameters from each of the animal-specific cases, are shown in Table 4.3. The maximum tension generated was found to be 212 ± 5.32 kPa. The pCa_{50} value at 2300 nm was found to be $6.34 \pm .02$, which is higher than when the sarcomere length is 1900 nm at $6.28 \pm .03$. This shows a leftward shift in the force-pCa curve, which is consistent with length-dependent activation at the cellular level (Mamidi, Gresham, & Stelzer, 2014; Marcucci, Washio, & Yanagida, 2017) (Figure 4.5). Also, the hill coefficients (n_H) showed a decreasing trend at longer sarcomere lengths, consistent with previous reports (Pulcastro et al., 2016). For a sarcomere length of 1900 nm, $n_H = 4.02 \pm 0.08$ but for 2300 nm, $n_H = 3.31 \pm 0.07$. Finally, the ktr values are consistent with

25

extrapolated values from the literature (de Tombe & Stienen, 2007), i.e., previous experiments report values at temperatures increasing from 15°C to 25°C. The current results ($ktr_{max} = 77.07 \pm 4.89$ s^{-1} and $ktr_{min} = 18.58 \pm 5.45$ s^{-1}) are meant to represent in vivo function, where the temperature would be 37°C.

Table 4.2: Optimized Active Parameters

	Case 1	Case 2	Case 3	Case 4	Case 5
k_{on} [M^{-1} s^{-1}]	5.0e7	5.0e7	5.8e7	5.0e7	8.0e7
k_{off} [s^{-1}]	90.00	70.00	95.00	76.01	115.01
k_1 [s^{-1}]	6.02	7.70	8.00	9.15	6.50
k_2 [s^{-1}]	61.18	92.88	96.01	150.00	95.01
$k_{4,0}$ [s^{-1}]	615.49	900.00	490.82	510.74	381.41
$k_{4,1}$ [nm^{-4}]	1.84	2.00	8.66	14.33	16.78
k_{coop} [No Units]	5.00	4.02	4.00	4.00	4.00
x_{ps}** [nm]	5	5	5	5	5
k_{force}** [N^{-1} m^{-2}]	8e-5	8e-5	8e-5	8e-5	8e-5
k_3** [nm^{-1} s^{-1}]	1000	1000	1000	1000	1000

*Parameter values for the three-state cellular contraction model for all five models. ** denotes values that were set, and not varied as part of the optimization.*

Table 4.3: Single Cell Validation

	Case 1	Case 2	Case 3	Case 4	Case 5
T_{max} [kPa]	218.4	193.8	219.3	206.5	222.5
ktr_{max} [s^{-1}]	69.70	77.19	83.08	79.16	76.25
ktr_{min} [s^{-1}]	17.39	24.44	14.81	23.99	12.29
n_H	3.27	3.39	3.13	3.52	3.25
pCa_{50}	6.32	6.29	6.36	6.31	6.42

Single cell FE simulation results for a sarcomere length of 2300 nm using the three-state model. Tmax represents the maximum tension generated by the half-sarcomere at saturated calcium. ktrmax and ktrmin are the maximum and minum rates of force recovery, nH is the Hill-coefficient for the fit of the force-pCa curves, and pCa50 is the pCa at which the cell generates a tension equal to half of Tmax.
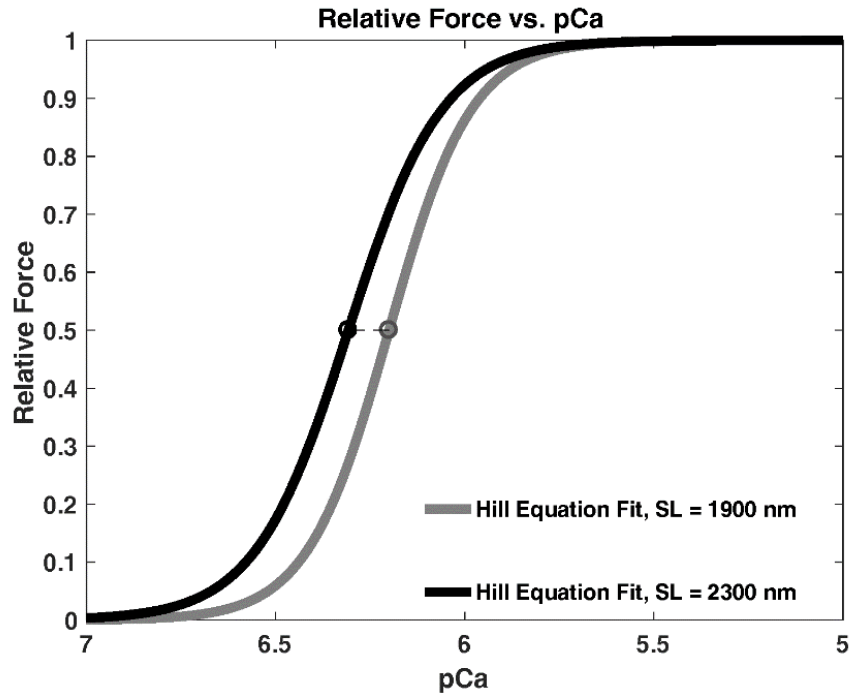
Figure 4.5: Model Force vs. pCa Curves. Representative single element FE predicted force at varying pCa values showing that as sarcomere length increases, the force vs. pCa curve shifts left, which captures the effect of length-dependent activation. The circles indicate the value at pCa50. Material from: Mann, Lee, Campbell & Wenk, Force-Dependent Recruitment From Myosin OFF-State Increases End-Systolic Pressure-Volume Relationship in Left Ventricle, Biomechanics and Modeling in Mechanobiology, published 2020, Springer-Verlag GmbH Germany, part of Springer Nature.

4.4: Discussion

Frank-Starling is an important mechanism for beat to beat regulation of contraction in the heart. Length dependent activation (LDA) at the cellular level is an important underlying mechanism for this, and work has shown that passive force and mechanosensitive transitions in the thick filament may be responsible for LDA (Ait-Mou et al., 2016; Fukuda, Sasaki, Ishiwata, & Kurihara, 2001). The current model incorporates a novel three-state contraction scheme, which includes a myosin SRX state and a force-modulated transition out of this state, into an organ level FE model. This model is able to reproduce experimentally measured pressure and wall deformation during the cardiac cycle. Thus, the framework can make predictions regarding organ level function by considering cell level mechanisms, traversing the scale between sarcomeric function and ventricular function.

This three-state contraction model, while not capturing all of the biochemical pathways of cross-bridge cycling, is able to incorporate many important aspects of muscle contraction including interfilamentary movement, the cooperative nature of thick and thin filament binding, and strain dependence of cross-bridge kinetics. Compared to the previously embedded two-state model, the current model has fewer parameters that required optimization during the fitting procedure (Xiaoyan Zhang et al., 2018). This decreased the time needed to run a numerical optimization while still utilizing a more intricate contraction scheme. This is advantageous for future translation of this technique to clinical data.

The current approach is able to reproduce LDA in a physiologically realistic way, shown at the cellular level as a leftward shift in the force-pCa curve (Figure 4.5). Additionally, the maximum isometric contraction that is generated at the cellular level was higher with the three-state model. As reported previously (Xiaoyan Zhang et al., 2018), the maximum contractile stress generated by the two-state model was 135.3±5.2 kPa. In the current work, the maximum contractile stress generated by the three-state model was 212.1±11.9 kPa. Considering that both models generate zero stress when the sarcomere length is reduced to the slack length, it can be inferred that the slope of the stress-length relation is steeper for the three-state model. That is, for the same sarcomere length and level of calcium, the presence of force-dependent recruitment leads to higher contractility. Both the force-pCa and stress-length relations suggest that force-dependent recruitment from the SRX-state at the cell level produces a steeper ESPVR at the organ level.

In order to confirm that these results are caused by force-dependent recruitment, and not just the presence of the SRX-state, PV loops were generated with the k_{force} parameter set to zero and the k_1 parameter increased. When this was done, the ESPVR dropped to a value in line with the two-state model. This implies that force-dependent recruitment is a critical factor in ESPVR. As the sarcomere is passively stretched, myosin heads are recruited into the myosin DRX-state, which during contraction increases the overall number of force-generating cross-bridges leading to a higher active stress (Table 4.3). In the two-state contraction model, all myosin already exists in the myosin DRX state, restricting the length dependence of the number of cross-bridges to the overlap of the thick and thin filaments.

It should be noted that in our previous work, the two-state model was compared to a phenomenological contraction model (time-varying elastance) (Xiaoyan Zhang et al., 2018). It was found that the phenomenological model was unable to reproduce the experimentally measured pressure profiles, and thus did not converge during the optimization. In addition to this deficiency, phenomenological models are unable to represent the presence of the SRX-state, which has been shown to play a role in the development of heart disease (Kampourakis, Ponnam, & Irving, 2018). Thus, these models may not be able to capture the effects of this cellular mechanism on organ level function.

A further improvement to the current model is the advancement of the passive material constitutive law. Previously, the entire passive response of the cardiac tissue in the FE model was represented by the bulk tissue (Xiaoyan Zhang et al., 2018). However, during contraction, much of the tissue response is compression and myofibers cannot bear a compressive load. This affected the force-dependent recruitment of myosin, especially during the latter half of systole as the magnitude of compression increases. This motivated the decomposition of the passive response discussed above, which resolved this issue and advanced the model more towards a structural model rather than phenomenological.

Finally, it was shown that this three-state implementation is able to predict mid-ventricular end-systolic strains reasonably well when compared to experimentally obtained strains. While the longitudinal strain component from the three-state implementation was statistically different than experimental data, it was also statistically different from the two-state implementation and closer to the CMR value. This implies that while not perfect, the predicted strain for this component was improved and trending toward the experimental data.

There are still limitations associated with this model. This includes the lack of bidirectional coupling between the intracellular calcium and the cross-bridge kinetics, as cross-bridge kinetics do not impact the calcium transient. This will be investigated in future studies. While the passive material law has been improved, allowing for a more accurate representation of stress within a myofiber, the law is still not fully structurally-based (Xi

et al., 2019). This will be addressed in the next iteration of this modeling framework. Finally, future FE models will include the right ventricular geometry and loading in the model.

This work shows how multiscale modeling can test hypotheses regarding cell level mechanism on organ level function, specifically the relationship between the myosin SRX-state and ESPVR. By representing active contraction in a way that captures realistic cross-bridge distributions, this approach advances the field towards mechanistic models rather than phenomenological models, displaying greater predictive power without sacrificing fits to experimental data. In addition, recent work has exposed the importance of this force-dependent transition of myosin heads and suggests perturbations to this transition may be important in the development of cardiac hypertrophy (Kampourakis et al., 2018). This is a significant step in advancing the relevance of computational modeling toward its potential of predicting cardiac function in diseased states or with potential interventions (Campbell et al., 2019).

CHAPTER 5: IMPACT OF DISARRAY ON FIBER MECHANICS, KINETICS

5.1: Background

Muscle cells are categorized as either smooth muscle, cardiac muscle, or skeletal muscle. Though different in function, healthy cardiac and skeletal muscle tissue are highly organized into locally parallel myofibers, which are in turn further organized into parallel sarcomeres, the basic unit of contraction. This organization and its maintenance are critical for the efficient transmission of force generated during contraction and is an active field of study. Disruption of this structure in turn disrupts function, as seen for example in hypertrophic cardiomyopathy (HCM) (Finocchiaro et al., 2021), myocardial infarction (Zimmerman, Criscione, & Covell, 2004) and in various mutations seen in the myosin heavy chains (Martinsson et al., 2000). For this study, skeletal muscle fibers will be considered.

Finite element modeling has been extensively used to model muscle tissue. Though they have grown in their sophistication, rigorous multiscale models that bridge cell level mechanisms and tissue function are still relatively new. Further, computational modeling of growth and remodeling of myofiber reorientation is relatively new. Much of the work focuses on potential mathematical measures to use to capture fiber remodeling but is limited by only considering passive mechanics or attempts to explain the development of healthy geometries.

This study is a systematic evaluation of the effects of disarray on muscle mechanics. Specifically, a physiologically inspired active contraction model is used in the formation of a 3D, multiscale model that is capable of linking fiber disarray to active force generation, myosin kinetics, and the efficiency of striated muscle. A novel framework (MyoFE) consisting of a Huxley-type cross-bridge model embedded into implicit finite element code is used to model a representative striated muscle fiber. Simulations show that the model can produce a realistic skeletal muscle fiber twitch profile. Quantifiable degrees of random disarray are introduced in the in-situ fiber. Results from simulations of isometric twitches and loaded shortening show that as disarray increases, peak active stress is significantly

diminished, muscle efficiency is decreased, and relaxation rates are increased. This multiscale model quantifies the effects that myofibril disarray has on muscle function, and capable of predicting muscle efficiency.

5.2: Methods

The MyoFE framework described in chapter three is used for this study along with the 4-state kinetic MyoSim scheme (Figure 2.3). For this study, x-domain of the force-generating state was discretized into $n = 21$ intervals, as further refinement does not impact results and is more computationally expensive. Time was discretized into 0.5 ms time steps, and Newton's method used to solve a backward Euler integration scheme. For each time step, the active contraction model is solved to yield the relative myosin populations based on the current intracellular calcium concentration $[Ca^{2+}]$ and half-sarcomere length. Note, T, the active stress calculated from MyoSim shown in chapter two, has a spatial dependence and is updated during each iteration of the Newton method.

A cylindrical geometry consisting of 1168 tetrahedral elements was created using Gmsh (Geuzaine & Remacle, 2009) (Figure 5.1 (a)). At each integration point, f_0 was assigned by selecting its cartesian coordinates from a gaussian distribution of width w, where w varies linearly from 0 at the surface of the fiber to some maximum value in the center. The resultant fiber vectors are then normalized. The results in fiber directions that are tangent to the surface of the fiber and become increasingly disorganized towards the center of the fiber. The distribution was centered at 1 for the x-component, and 0 for the y and z-components. This results in a vector aligned parallel to the fiber long axis when w is 0 (Figure 5.1(b)) and introduces random disarray as w increases (Figure 5.1(c)). For this study, w is chosen from the set $W_G = \{0, 0.25, 0.50, 0.75, 1.0, 1.25, 1.50\}$. Finally, ρ (the cross-bridge density) is set to zero for all integration points within the first and last 10% of the fiber to create non-contractile tissue. This allows for contraction against a non-linear compliant region to mimic a connection to connective tissue (Campbell, 2016). The passive material parameters were selected to obtain an average half-sarcomere shortening of ~8% during an isometric twitch.
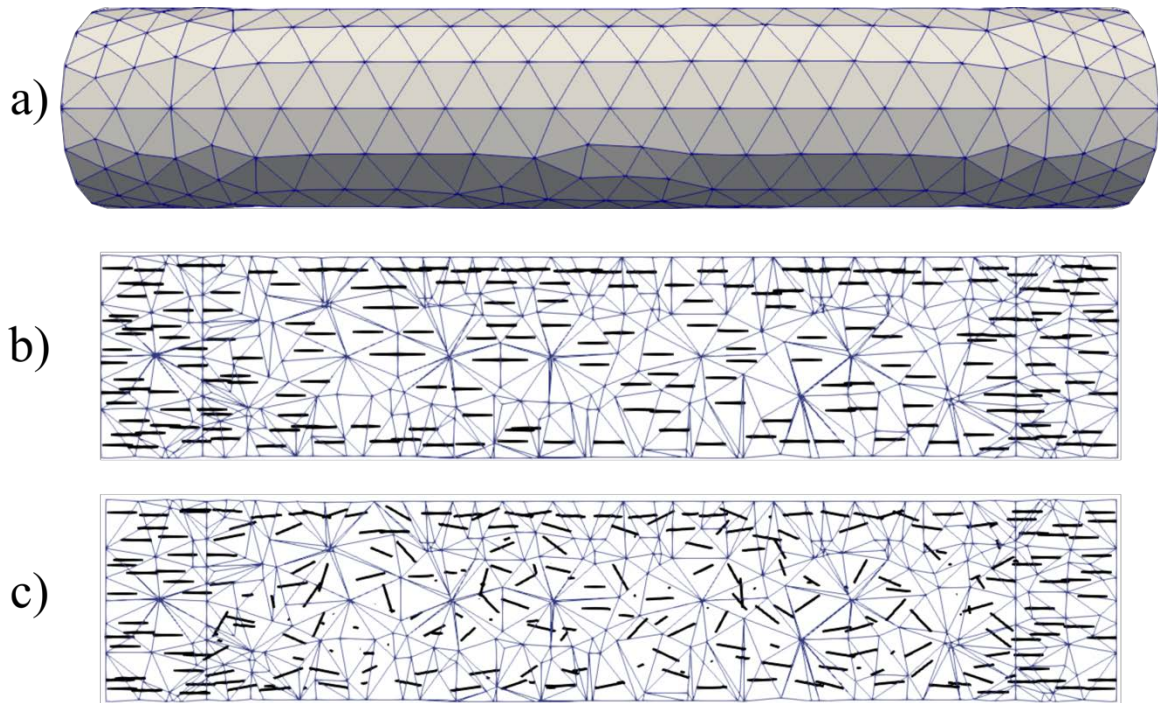
Figure 5.1: Mesh Geometry & Representative Disarray. (a) Cylinder tetrahedral mesh created with GMSH used for all simulations, (b) random sampling of fiber orientations in a cross-section through the center showing all fibers aligned with the long axis and (c) disarray induced by selecting f0 components from a gaussian distribution of width 1.50. Note that the fibers in the compliant regions remain aligned.

Each simulation in which disarray is present was repeated with ten different random seed values when assigning fiber distributions. Active contraction parameters were chosen to reproduce max stress and time to half-relaxation (time from peak stress to 50% stress as measured from the steady state stress prior to activation) from the literature (Gonzalez, Messi, & Delbono, 2000) for the case $w = 0$.

Isometric Twitch

An isometric twitch simulation was performed to measure changes in peak stress and myosin kinetics induced by disarray. Note, in this context isometric refers to overall fiber length and not individual half-sarcomere length. To simulate an isometric twitch, the right face of the fiber is displaced 5% to induce a non-zero resting tension. This displacement boundary condition remains constant for the duration of the simulation such that the overall fiber length (the length of the contractile tissue and connective tissue) remains fixed. A two-compartment calcium model is used to calculate $[Ca^{2+}]$ at each time step. The two

compartments in the calcium model are intracellular calcium (Ca) able to bind to troponin, and calcium stored in the sarcoplasmic reticulum (Ca_{SR}). k_{leak} is a rate constant representing the slow leak of calcium into the cytoplasm, k_{act} is the rate of calcium influx due to activation, k_{serca} represents the rate at which calcium is pumped back into the sarcoplasmic reticulum. The term $activation$ is a scalar that represents the depolarization state of the cell, taking values of 0 for polarization and 1 for depolarization. Parameters were chosen to replicate a fast-twitch skeletal muscle transient (Baylor & Hollingworth, 2003). Prior to activation, intracellular calcium is at a steady state value of 1×10^{-7} M. At $t = 300$ ms, the muscle is activated, allowing time for myosin populations to reach steady state. The simulation was repeated for all values in W_G.

$$\frac{dCa}{dt} = (k_{leak} + (activation)k_{act})Ca_{SR} - k_{serca}Ca$$
$$\frac{dCa_{SR}}{dt} = -(k_{leak} + (activation)k_{act})Ca_{SR} + k_{serca}Ca$$

Loaded Shortening

Loaded shortening simulations were performed to calculate the work a fiber can do against a range of afterloads, ranging from 10% to 90% of the peak stress obtained during an isometric twitch. This work, along with calculated myosin-ATPase was used to calculate a cross-bridge efficiency of the fibers. The loaded shortening simulations are identical to the isometric twitch simulations for the first 300 ms, the time at which activation begins. Once the resultant force in the long axis direction on the right face reaches the desired afterload, an equivalent traction was prescribed on that face allowing for the length of the fiber to change, specifically to shorten. This traction is maintained on the right face until shortening can no longer be maintained by active contraction and maximum shortening has been reached. Once maximum shortening has been reached, the traction is set to zero and the displacement obtained by the right face at maximum shortening is enforced for the remainder of the simulation, keeping the fiber at its shortest length, allowing relaxation to occur and preventing re-lengthening from influencing relaxation (Chung et al., 2017). Efficiency is calculated as the ratio of work to myosin ATPase:

$$Myosin\ ATPase = \frac{\pi\rho(L_{fiber}) * \Delta G' * \sum_{N_G} \sum_{i=1}^{21} J_7(x_i)}{L_0 N_A N_G}$$

$$Work = F_{end} u_{end}$$

where ρ is the density of half-sarcomeres in contractile tissue, $\Delta G'$ is the free energy produced by ATP hydrolysis, L_{fiber} is the length of the fiber, L_0 is the reference half-sarcomere length, N_A is Avogadro's number, N_G is the number of integration points, and the summation is the sum of fluxes out of $M_{FG}(x)$ to M_{DRX} over N_G. F_{end} is the sum of the nodal forces on the right face of the fiber, and u_{end} is the maximum displacement of the right face of the fiber.

5.3: Results

Parameters used in all simulations can be found in Table 5.1 and Table 5.2:

Table 5.1: Passive Material Parameters

Passive Material Parameters		
	Contractile Region	Compliant Region
c	400	400
c_2	50	50
c_3	8	3
b_f	10.48	3
b_t	3.58	3.58
b_{fs}	1.627	1.627

Table 5.2: Kinetic Scheme Parameters

Kinetic Scheme Parameters	
k_1	6.0
k_{force}	2.5e-4
k_2	280.0
k_3	440.0
$k_{4,0}$	667.0
$k_{4,1}$	1.0
$k_{5,0}$	1400.0
$k_{5,1}$	0.1
k_6	0.0
$k_{7,0}$	143.0
$k_{7,1}$	0.2
k_8	0.0
k_{on}	5.1e8
k_{off}	180.0
k_{coop}	4.0

Statistics

Statistical tests were performed to look for significant differences between all values in the set W for plotted quantities. The Shapiro-Wilk test was used to check for normality of data. Levene's test was used to test for homogeneity of variances between disarray groups. One sample t-tests were performed to test for differences between the means of groups with normal data and the value calculated in the aligned simulation. In the case of deviations from normality, the one sample Wilcoxon test was used. To test for differences between disarray groups, a one-way ANOVA was used when all populations satisfied normality and homogeneity of variances, followed by Tukey's posthoc test if needed. In the case that only homogeneity of variances was violated, a Welch's ANOVA was performed. In cases where the assumption of normality was violated in any disarray group, the Kruskal-Wallis test was performed with a Dunn's posthoc test if needed. Alpha was set to 0.05, and Bonferroni corrections performed to correct for multiple t-tests.
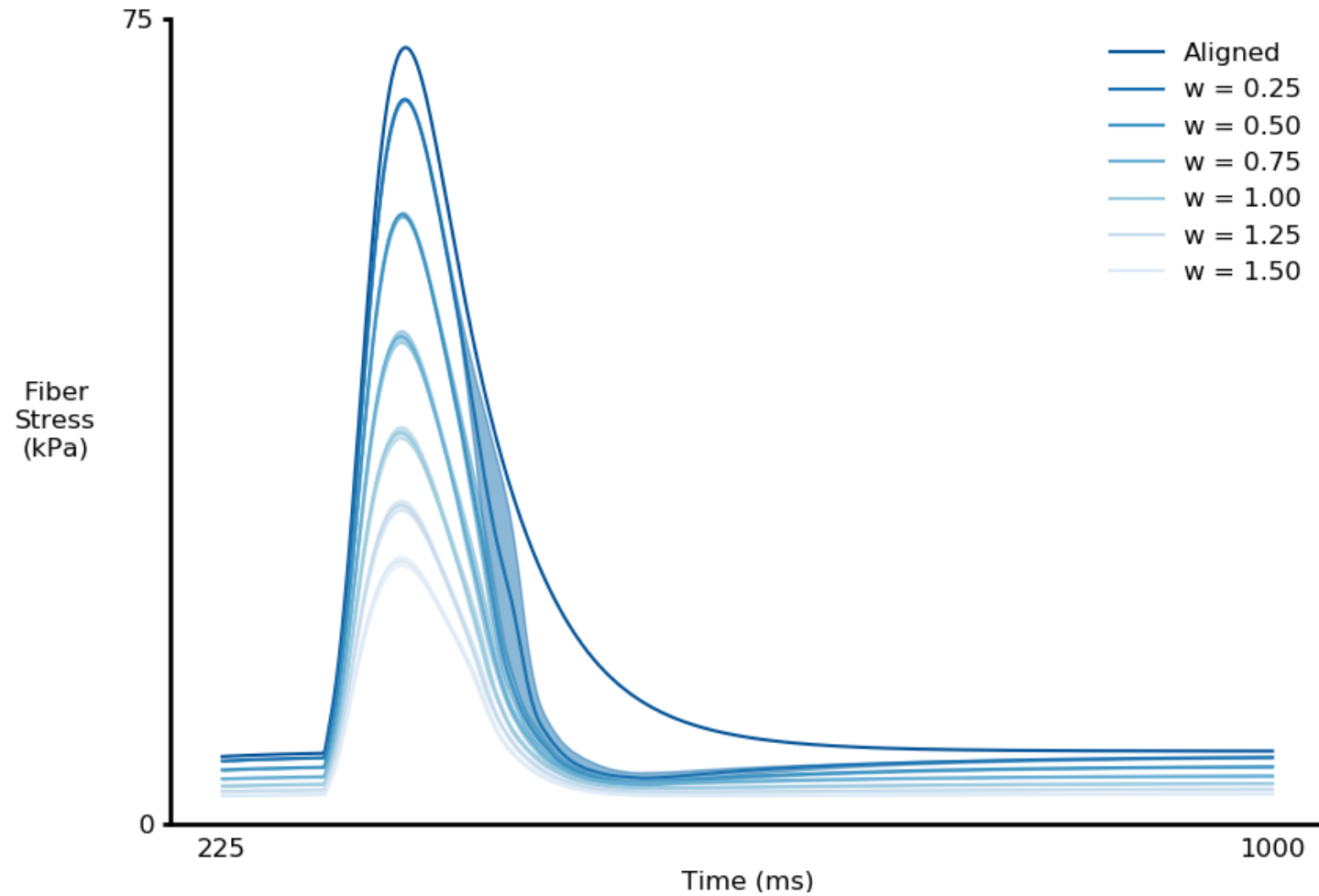
Figure 5.2: Fiber Stress vs. Time. Total fiber stress as a function of time. Traces are mean +/- standard deviation as calculated from results of 10 simulations with different random seeds.
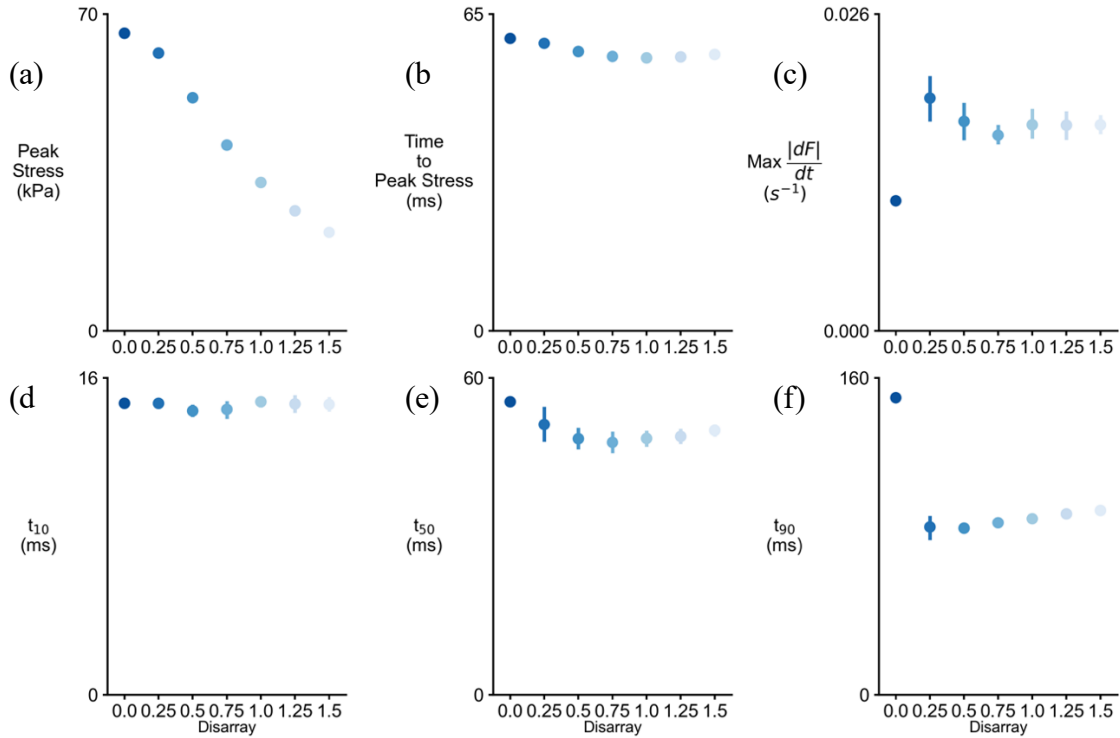
Figure 5.3: Twitch Kinetics. (a) Peak stress, (b) Time from activation start to peak stress, (c) maximum rate of relaxation as percentage of peak stress, (d) 10 % relaxation time (time to 90% of peak stress as measured from steady state stress), (e)half-relaxation time where half-stress is calculated from steady state to peak and (f) 90% relaxation time (time to 10% of peak stress as measured from steady state stress). Results presented as mean +/-standard deviation.

Significance Matrices

To avoid difficult to interpret bars on the results plots, matrices are used to indicate statistical differences between values. The asterisk symbol (*) in column *i*, row *j*, indicates a statistically significant difference between groups represented in the respective row and column for a corrected alpha value of $0.008\overline{3}$.

Table 5.3: Peak Stress

Peak Stress							
	0.00	0.25	0.50	0.75	1.00	1.25	1.50
0.00	–	*	*	*	*	*	*
0.25	*	–	*	*	*	*	*
0.50	*	*	–	*	*	*	*
0.75	*	*	*	–	*	*	*
1.00	*	*	*	*	–	*	*
1.25	*	*	*	*	*	–	*
1.50	*	*	*	*	*	*	–

38

Table 5.4: Time to Peak Stress

Time to Peak Stress							
	0.00	0.25	0.50	0.75	1.00	1.25	1.50
0.00	-	*	*	*	*	*	*
0.25	*	-		*	*	*	*
0.50	*		-	*	*	*	
0.75	*	*	*	-			
1.00	*	*	*		-		
1.25	*	*	*			-	
1.50	*	*					-

All disarray peak stresses were found to be significantly different than the aligned fiber's peak stress, as well as significantly different from each other. The time to reach peak stress (t_{peak}) was found to be different for all disarray cases when compared to the aligned case. Looking at differences between disarray cases, the case of $w = 0.25$ was additionally found to be statistically different than the cases of w = 0.75, 1.00, 1.25 and 1.50. The case of w = 0.50 was found to be different than for w = 0.75, 1.00 and 1.25.

Table 5.5: Time to 10% Relaxation

t_{10}							
	0.00	0.25	0.50	0.75	1.00	1.25	1.50
0.00	-						
0.25		-					
0.50			-				
0.75				-			
1.00					-		
1.25						-	
1.50							-

Table 5.6: Time to 50% Relaxation

t_{50}							
	0.00	0.25	0.50	0.75	1.00	1.25	1.50
0.00	-	*	*	*	*	*	*
0.25	*	-					
0.50	*		-				
0.75	*			-			
1.00	*				-		
1.25	*					-	
1.50	*						-

Table 5.7: Time to 90% Relaxation

t_{90}							
	0.00	0.25	0.50	0.75	1.00	1.25	1.50
0.00	-	*	*	*	*	*	*
0.25	*	-					*
0.50	*		-			*	*
0.75	*			-		*	*
1.00	*				-		*
1.25	*		*	*		-	
1.50	*	*	*	*	*		-

Table 5.8: Maximum dF/dt

$\left(\dfrac{|dF|}{dt}\right)$							
	0.00	0.25	0.50	0.75	1.00	1.25	1.50
0.00	-	*	*	*	*	*	*
0.25	*	-					
0.50	*		-				
0.75	*			-			
1.00	*				-		
1.25	*					-	
1.50	*						-

Four different quantities were calculated to asses relaxation times: time to 10% relaxation (t_{10}), time to 50% relaxation (t_{50}), time to 90% relaxation (t_{90}), and the maximum magnitude of relaxation rate, calculated as the greatest decrease in stress per time-step as a percentage of peak stress $\left(\frac{|dF|}{dt}\right)$. No significant differences were found between any groups for t_{10}. All disarray cases were found to have significantly different t_{50} times from the aligned case, but no differences were found between disarray cases. All disarray cases were also found to have significantly different t_{90} times as compared to the aligned case. Furthermore, the cases of $w = 0.25$ and $w = 1.00$ were significantly different from the most extreme disarray case of $w = 1.50$, and the cases of $w = 0.50$ and $w = 0.75$ were significantly different from the cases $w = 1.25$ and $w = 1.50$. Finally, all disarray cases were found to have significantly different $\frac{|dF|}{dt}$ values when compared to the aligned case, but no differences were found between disarray cases.

Loaded Shortening

For each case, efficiency is zero for both unloaded shortening (representing no afterload) and isometric contraction because no work is done. Representative efficiency traces for each case are shown in Figure 5.5. The appropriate one sample test was performed to investigate differences in efficiencies between disarray cases and the aligned case for each afterload. One-way ANOVA was used to investigate differences in efficiencies between disarray cases for a given afterload.
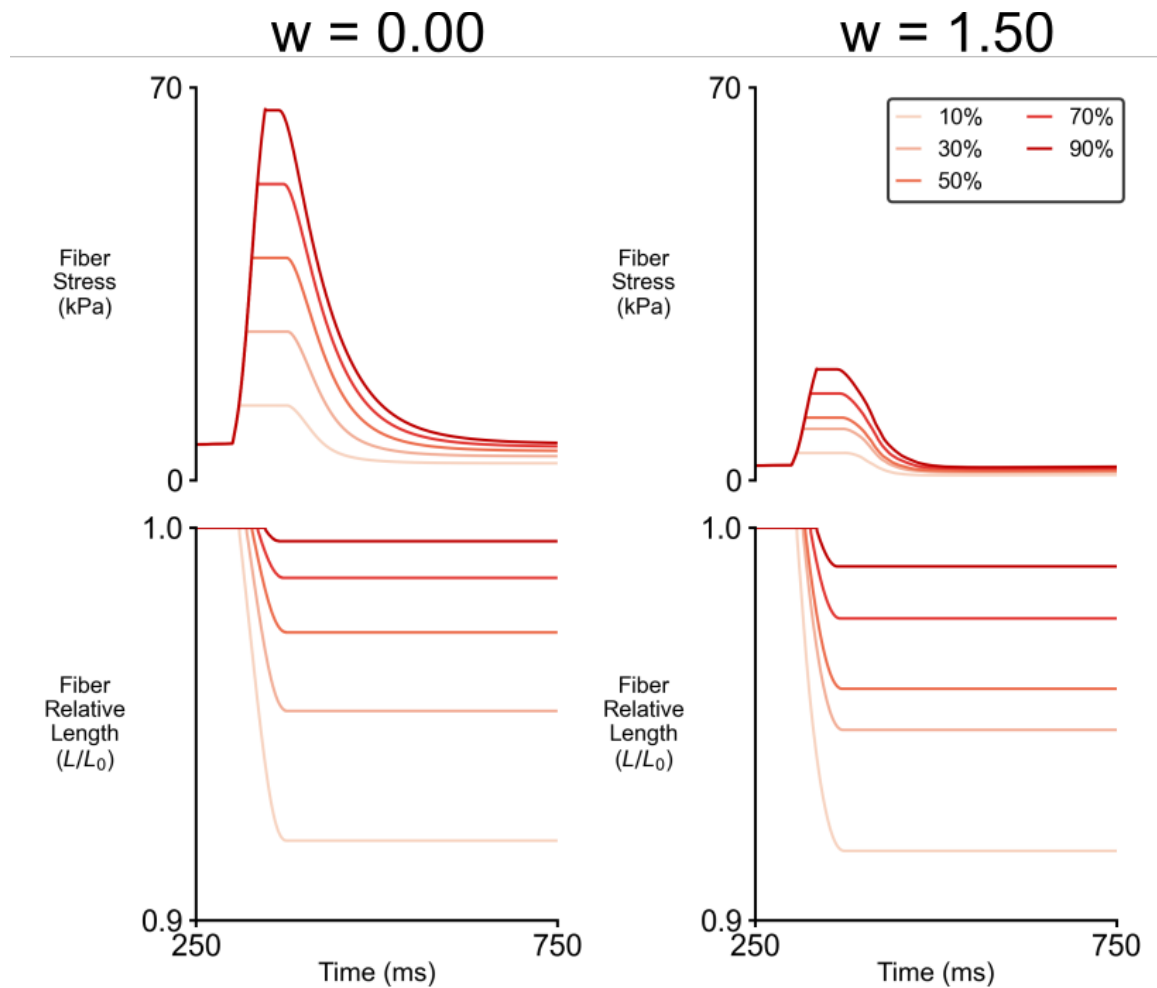

Figure 5.4: Fiber Force vs. Length. Representative plots showing fiber stress during loaded shortening simulations (top row) for the aligned fiber (left column) and most severe disarray case (right column), and the relative fiber length (bottom row).

41
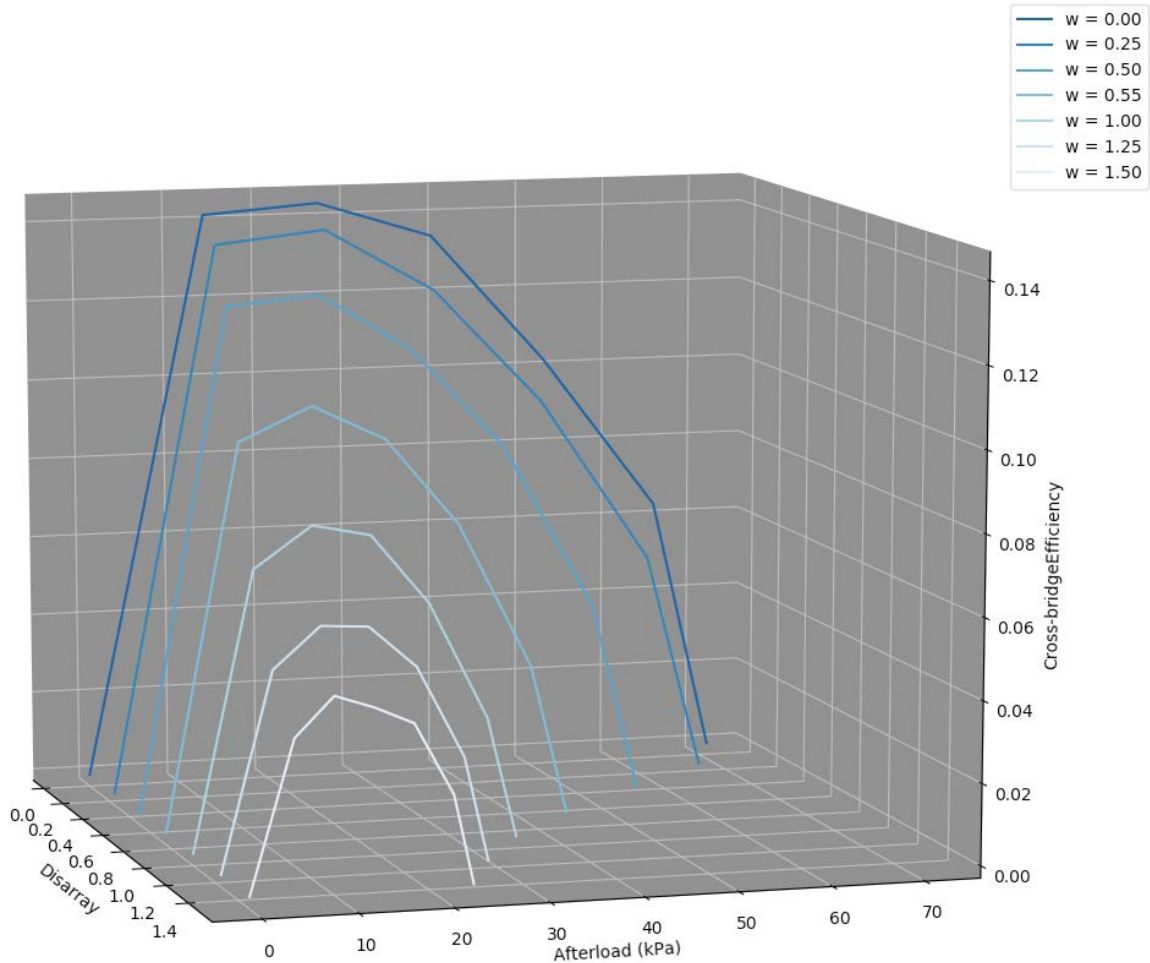
Figure 5.5: Efficiency vs. Disarray and Afterload. Representative 3D plot of cross-bridge efficiency vs. disarray and afterload. As disarray increases, fibers can shorten against a narrower range of loads at lower efficiencies.

For shortening against afterloads of 10-50%, all disarray cases were found to have statistically different efficiencies compared to the aligned case. For an afterload of 70%, all disarray cases were statistically different from the aligned case except for the case $w = 0.25$. For a 90% afterload, the cases $w = 0.25$ and 0.50 showed no statistical difference in efficiency when compared to the aligned case, but all other cases did.

For the 10% and 30% afterload simulations, all disarray cases were found to have statistically different efficiencies from one another. In simulations for shortening against 50%, 70%, and 90% afterload, the cases of $w = 0.25$ and 0.50 had a statistically different

mean efficiency than the cases of 1.00, 1.25, and 1.50, and the case w = 0.75 was statistically different from the most severe disarray case of w = 1.50.

5.4: Discussion

Decreased force production: This can be simply explained by the fact that fibers that are not aligned with the long axis only transmit a fraction of their force in the direction the reaction force is measured. Not only this, but fibers not aligned with the long axis experience less pre-stretch at the beginning, which has a significant effect on length-dependent activation (Campbell et al., 2018). Also, since the half-sarcomeres/myofibrils aren't aligned with the long axis, the initial pre-stretch is not felt by them and the mean overlap between thick and thin filaments is less, thus fewer binding sites are available for cross-bridge formation.

Relaxation: Relaxation is happening quicker in the disarray cases. This is seen in the half relaxation time, but even more drastically during the last half of relaxation (t_{90}). This is due to the half-sarcomeres experiencing rupture (Campbell, 2016). Note that the active stress being produced is matched by the passive response in the non-contractile tissue at the ends. One potential explanation could be that since the disarray fibers are producing less force, the passive tissue they are contracting against is sitting lower on the passive stress vs. strain curve. Therefore, the disarray fiber experiences a larger strain for a given reduction of stress in comparison to the aligned fiber. A recent study found that in heterogeneous myocardium, the faster relaxing cardiomyocytes dominate the overall relaxation behavior (Clark et al., 2021). This increased strain rate increases the relaxation rate leading to the occurrence of rupture, whereas the aligned fibers maintain a slow enough relaxation (in part due to the viscosity from the weakly bound cross-bridges) to prevent rupture.

Efficiency: Loaded shortening data is presented in Figure 5.6. In all loaded shortening simulations, the trend indicates that as disarray increases, the amount of work done decreases. Though the amount of shortening achieved is comparable, except for shortening against 10% afterload, the absolute force measured at the end of the fibers is diminished

with disarray as noted above. Not only does work decrease, energy consumption either remains constant across disarray values or increases, leading to the observed decrease in efficiency. Myosin ATPase is measured from the amount of heads detaching from the force-generating state and transitioning to the disordered-relaxed state. Therefore a higher myosin ATPase is a result of a higher average detachment of cross-bridges. Since the contraction parameters are the same for each simulation, it is likely that the strain-dependent nature of cross-bridge detachment is responsible for the higher energy consumption. As discussed in chapter two, in the MyoSim contraction model shortening velocity is governed by the proportion of cross-bridges that are strained into the region in which length change is resisted. In the case of a single half-sarcomere with a load P applied to the end, the net cross-bridge force is equal to this load. Shortening velocity is at a maximum for an unloaded twitch ($P = 0$). As myofibril alignment shifts from the fiber long-axis towards the traction free fiber surface, it is likely that shortening velocity increases, thus cross-bridge detachment increase, and myosin ATPase increases, or at the very least does not decrease.
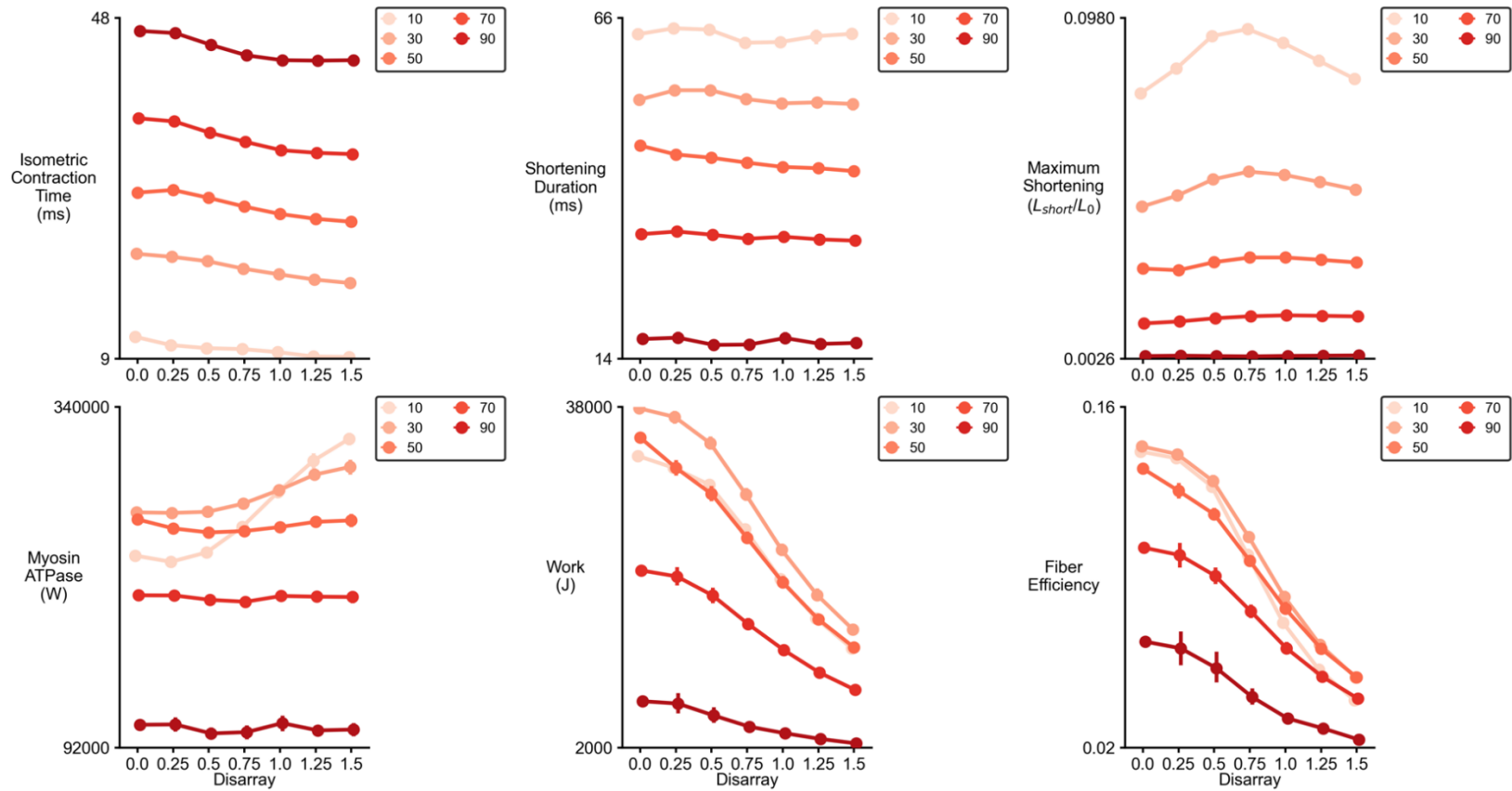
Figure 5.6: Loaded Shortening Analysis. Loaded shortening analysis. The independent variable in each plot is the amount of disarray, and results are colored according to the percentage of afterload prescribed.

CHAPTER 6: PRELIMINARY WORK ON GROWTH AND REMODELING

One of the goals of the MyoFE framework is to capture cardiac growth and remodeling. For this preliminary work, remodeling is restricted to just considering the changes in the reference fiber angle f_0, and not changes in material properties. Remodeling is simulated by adapting the method proposed by Kroon et al. (Kroon, Delhaas, Bovendeerd, & Arts, 2009) to consider different potential stimuli. Preliminary simulations show remodeling occurring in strips of tissue, and also show steady state orientations reached in an ellipsoidal simulation of the left ventricle. Cardiac growth is modeled using the volumetric growth theory approach in which the deformation gradient F is multiplicatively decomposed into an elastic a growth component. A preliminary simulation shows concentric growth due to a changed set point of the considered stimulus (end systolic total stress along f_0).

6.1: Fiber Remodeling

Methods

Consider again the local coordinate system as described in chapter two consisting of vectors $f_0, s_0,$ and n_0. It is assumed in this work that reorientation is governed by either the stress or strain along the fiber direction f_0, and that the sheet and sheet-normal directions reorient in such a way as to maintain an orthogonal coordinate system. Let F be the deformation gradient that maps from the reference configuration to the current configuration. Define E to be the Green-Lagrange strain, which is given as

$$E = \frac{1}{2}(F^T F - I)$$

where I is the identity tensor. Finally, from chapter two, define S to be the passive second Piola-Kirchhoff stress tensor, and S_P the passive second Piola-Kirchhoff stress tensor where

$$S = S_p + S_a$$

Let $\boldsymbol{G}$ represent a generic tensor. The general form of the governing differential equation for fiber remodeling is defined as

$$\frac{d\boldsymbol{f_0}}{dt} = \frac{1}{k}(\boldsymbol{G} * \boldsymbol{f_0} - \boldsymbol{f_0})$$

where k is a time constant. It should be noted that $\boldsymbol{f_0}$ is normalized after each update. This differential equation is implemented in the MyoFE framework as a simple forward Euler step that occurs at the end of each time step.

Simulation Protocols

Two simulations are considered. First, a rectangular prism representing a "strip" of contractile tissue in which one end is considered compliant that undergoes cyclic activation to mimic cardiac cycles in the presence of heterogeneity due to fibrosis. Second, a truncated ellipsoid is used to simulate left ventricular cardiac cycles.

For the cyclically activated strip of tissue, active and passive parameters, the calcium transient, and prescribed afterload and end-diastolic values were adapted from a previous study simulating rat myocardium (Mann, Lee, Campbell, & Wenk, 2020). Diastole was mimicked by imposing a linearly increasing traction on the right face to a value of 4 kPa over 75 ms. Then, isovolumic contraction was modeled by fixing the displacement of the right face during activation until the calculated resultant stress reached the prescribed afterload of 30 kPa. At this point, a traction of 30 kPa was imposed on the right face, allowing the strip of tissue to shorten to mimic ejection. Finally, once this afterload could not be sustained by active contraction and re-lengthening started to occur, the traction boundary condition is removed and displacement of the right face fixed to allow for relaxation. Once the resultant stress difference between time steps fell below a tolerance of 5 Pa, diastole was simulated and the next cardiac cycle begins. For this simulation, fibrosis was modeled by randomly selecting contractile elements to be converted to fibrotic elements. Fibrotic elements were assigned to have a cross-bridge density of zero, and

passive parameters chosen to yield a tissue that is 20 times stiffer than contractile tissue, and isotropic.

In ventricle simulations, parameters were again adapted from myocardium (Mann, Lee, Campbell, & Wenk, 2020) to produce a steady state pressure volume loop after five cardiac cycles with similar diastolic and ejection pressures, cavity volumes, and an ejection fraction of ~61% prior to the introduction of fiber remodeling. After steady state was reached, five more cardiac cycles were simulated in which fibers were allowed to change orientation based on the remodeling differential equation.

Preliminary Results

In contractile strip simulations, each stimulus led to remodeling. The initial and final orientations are shown in Figure 6.1 along with the finite element mesh showing fibrotic elements versus contractile elements.
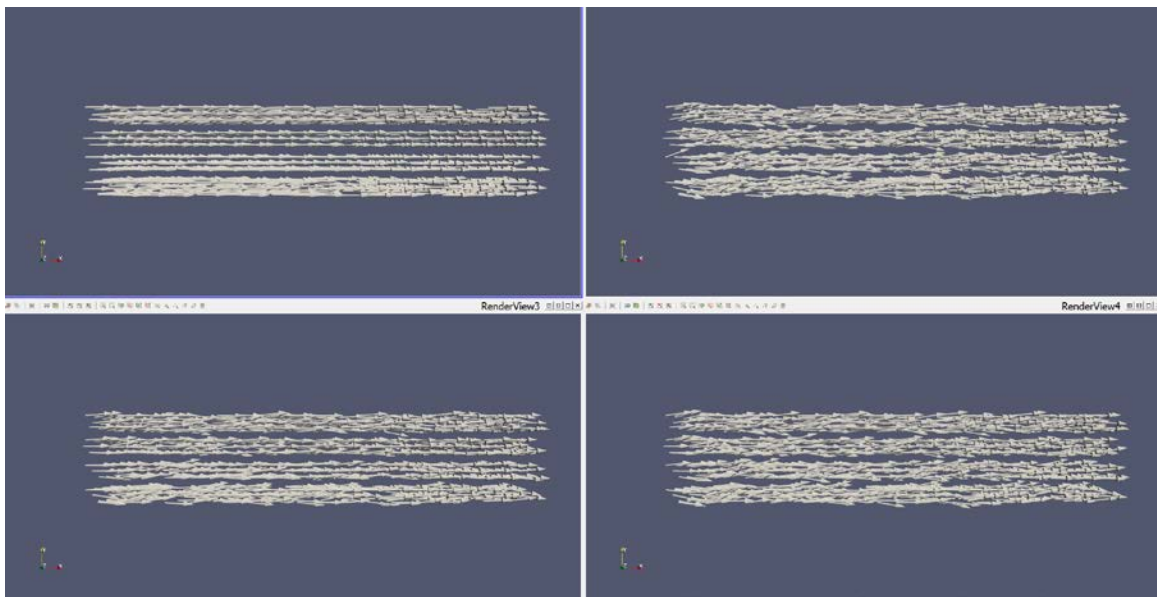

Figure 6.1: Initial and Final Fiber Orientation. (top left) Initial fiber distribution and final fiber distributions obtained for strip simulations in which remodeling was driven by $\mathbf{S_p}$ (top right), $\mathbf{S}$ (bottom left), and $\mathbf{E}$ (bottom right).

Histograms showing the degree of remodeling are shown in Figure 6.2. Qualitatively, reorientation driven by S (panel (b)) showed the least remodeling, and reorientation driven by S_p was similar to that obtained in the simulations driven by E.
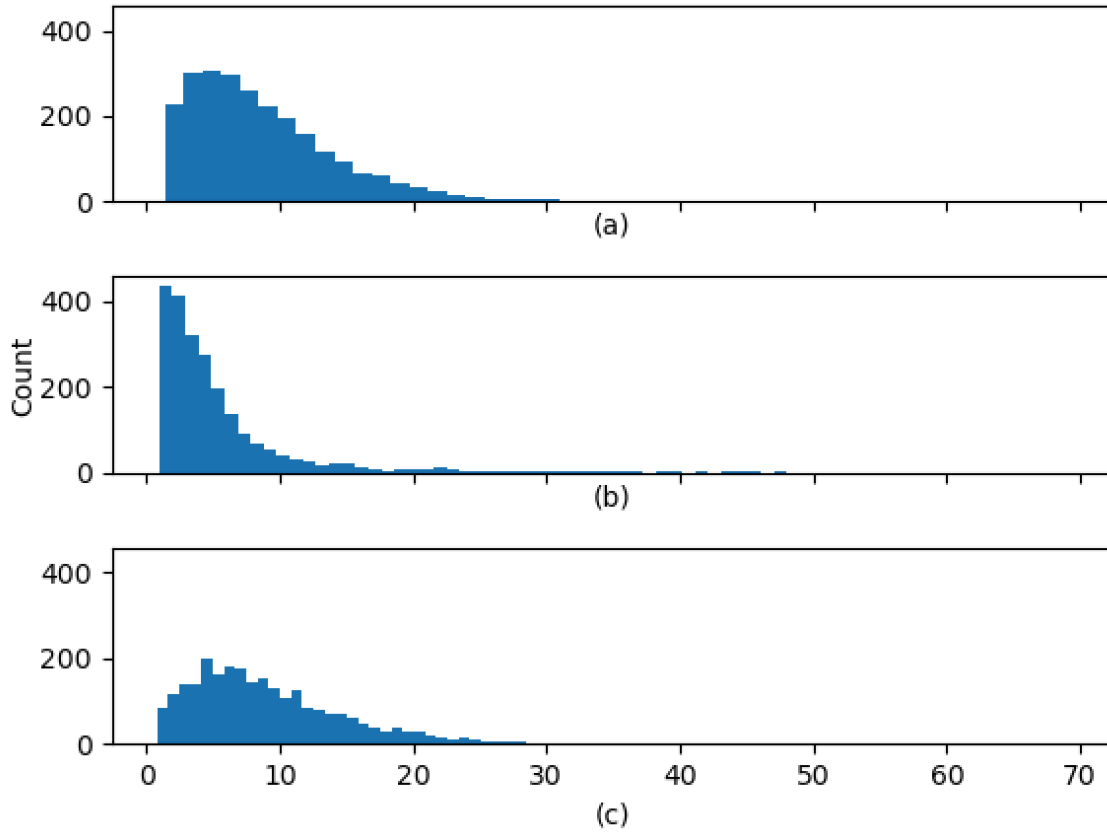
Figure 6.2: Reorientation Histograms. Histograms depicting final fiber angles measured in degrees from their initial orientation (the strip long axis) for the (a) passive stress tensor based reorientation, (b) total stress tensor and (c) Green-Lagrange strain tensor. Bin values represent the total number of vectors found calculated in the range of angles away from the long axis.

In the ellipsoid simulations, some remodeling did occur. Most remodeling occurs at the base such that shear stresses are minimized at the boundary. This is most likely caused by the boundary condition used at that base. Other notable remodeling occurs at the apex where the fibers spiral in towards the bottom point. All simulations reached a steady state configuration and qualitatively maintain orientations near the original distribution a linear variation between -60° at the epicardium and +60° at the endocardium. This implies that

the reorientation laws can represent realistic in vivo fiber distributions in the left ventricle. Original and final distributions are shown in Figure 6.3.
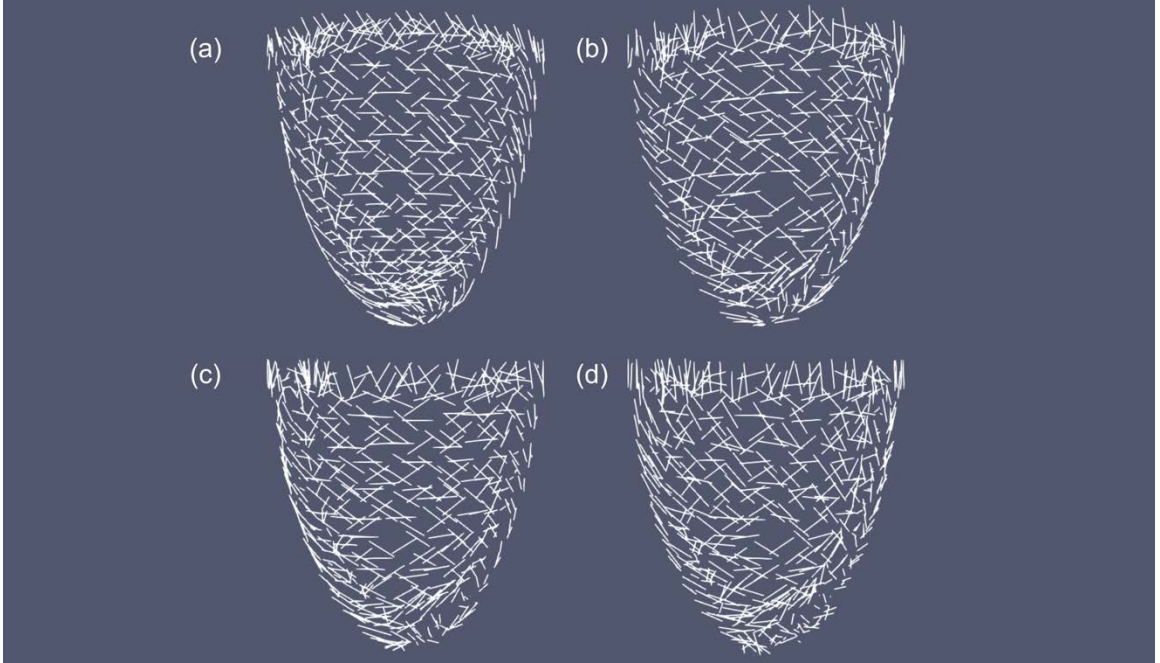

Figure 6.3: Ventricle Reorientation. Sampling of initial fiber orientation (a), and final fiber orientations after remodeling driven by $\mathbf{E}$ *(b),* $\mathbf{S}_\mathrm{p}$ *(c) and* $\mathbf{S}$ *(d).*

6.2: Growth

One of the most prevalent frameworks in modeling growth is that of volumetric growth. Utilizing the idea of a multiplicative decomposition of the deformation gradient $\boldsymbol{F}$ from plasticity, Rodriguez et al. (Rodriguez, Hoger, & McCulloch, 1994) proposed splitting the deformation gradient as

$$\boldsymbol{F} = \boldsymbol{F}_e \boldsymbol{F}_g$$

In this way, local changes in mass can be specified directionally via the inelastic growth tensor $\boldsymbol{F}_g$. Applying $\boldsymbol{F}_g$ maps the reference configuration β^0 to an intermediate configuration β^* due to the stress free removal or addition of material. Conventionally, addition in the fiber direction represents the serial addition of sarcomeres, while addition in the sheet and sheet normal directions represent the parallel addition of sarcomeres. In general however, β^* is not guaranteed to be physically compatible meaning gaps and overlaps can form. Compatibility is restored by applying an elastic deformation $\boldsymbol{F}_e^*$ that

restores continuity in the absence of any external loads, leading to residual stresses. In fact this framework has been used to model the existence of residual stresses observed in vivo (Alastrue, Pena, Martinez, & Doblare, 2007; Genet et al., 2015; Skalak, Zargaryan, Jain, Netti, & Hoger, 1996). The total current configuration β is achieved by applying $\boldsymbol{F}_e$ to the intermediate configuration β^*. As growth occurs, $\boldsymbol{F}_e$ is altered, changing the stress response of the tissue for a given load.
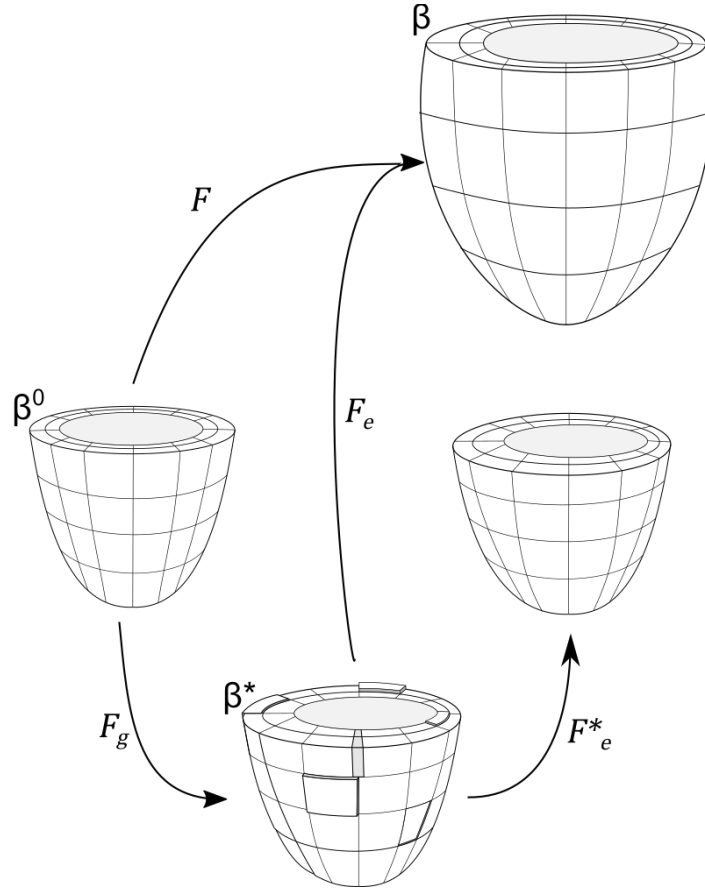
Figure 6.4: Growth Configurations. Schematic showing how $\mathbf{F_e}$, $\mathbf{F_g}$, $\mathbf{F_e^*}$ and $\mathbf{F}$ map between configurations. Ultimately $\mathbf{F}$ maps from the reference configuration β^0 to the loaded, grown and deformed configuration β. $\mathbf{F_g}$ maps from β^0 to β^* representing the stress free removal or addition of material. This configuration is not necessarily compatible, as shown via discontinuities and overlaps here. Compatibility is restored to via $\mathbf{F_e^*}$ to a new unloaded geometry. Finally, $\mathbf{F_e}$ maps from the incompatible grown configuration β^* to the final loaded configuration β.

For a preliminary growth simulation, total end systolic stress was used as a stimulus for growth in the $\boldsymbol{s_0}$ and $\boldsymbol{n_0}$ directions, resulting in concentric hypertrophy. Using the same ellipsoid ventricle steady state simulation previously described, the set point was defined

as 90% of the end-systolic total stress achieved in the steady state simulation. The unloaded ventricle geometry was grown over a sequence of 10 virtual growth steps (independent of time). This grown mesh was set as the new reference configuration, and five cardiac cycles simulated. This resulted in the grown ventricle and a new steady state pressure volume loop are shown in Figure 6.5.
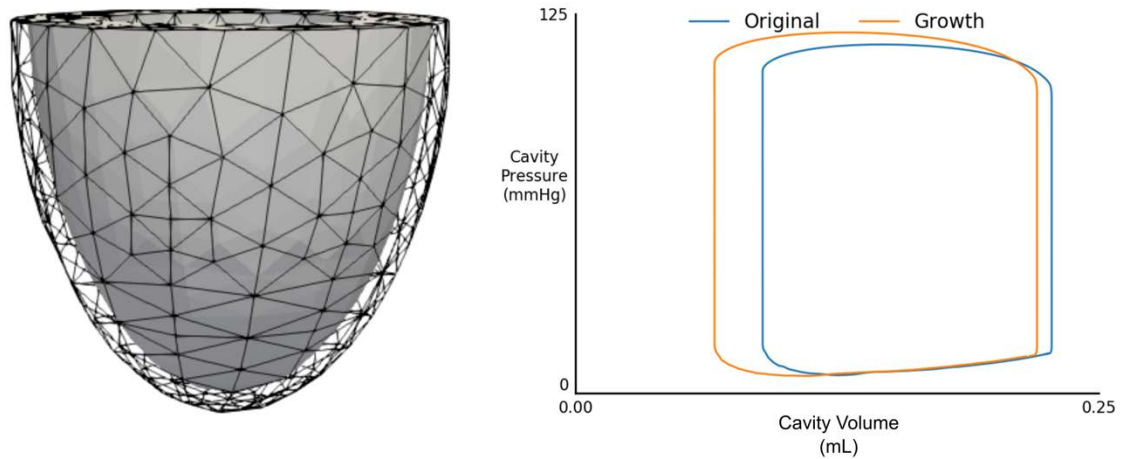

Figure 6.5: Preliminary Growth Results. (left) original mesh in gray inside a wireframe depiction of the grown mesh, and (right) steady state pressure volume loops for the original mesh (blue) and grown mesh (orange).

Future Directions

Preliminary results do not suggest that one stimulus for fiber remodeling is clearly better than any other. Future simulations will include simplified ellipsoid ventricle simulations in which heterogeneity is introduced in the form of diffuse fibrosis or heterogeneity of active or passive parameters. Ultimately, validation of a fiber remodeling law must include a comparison to experimental data in the form of histology or diffusion tensor magnetic resonance imaging.

For cardiac growth, the mechanisms to grow a mesh based on some input stimuli are established. Further refinement of simulations in which growth occurs, including honing of growth timing parameters, and the incorporation of a baroreflex are to be considered. Validation of these growth mechanisms will include comparison of growth of animal

specific finite element meshes to that measured via cardiac magnetic resonance imaging from a colony of mice including the R403Q mutation.

CHAPTER 7: CONCLUSION

In summary, this work consists of successfully implementing a physiologically motivated cell contraction model into two separate finite element frameworks. These frameworks are used to investigate both cell level and organ level function. In chapter four, the explicit framework with a three-state contraction scheme is used to investigate how force-dependent recruitment from the myosin super-relaxed state affects the end-systolic pressure-volume relationship and it is found that this recruitment increases this relationship. This may have implications regarding the Frank-Starling relationship, a crucial regulatory mechanism in the heart. In chapter five, a four-state kinetic scheme is used to simulate a skeletal muscle fiber to analyze the effects of myofibril disarray on function and efficiency. This study highlights the power of such a multiscale model, separating out the pure mechanical effects of disarray and perhaps most importantly, providing insights regarding the energy use required to sustain function in diseased muscle. It is the cell contraction model that allows for the connection between function and muscle energetics. In chapter six, preliminary work regarding cardiac growth and remodeling simulations is shown to highlight the mechanisms that are in place for future studies. This work will allow for the simulation of alteration in structure and function due to cardiac diseases such as hypertrophic cardiomyopathy.

Future investigations will include expanding the MyoFE framework to build a modular software that is capable of modeling cardiac growth and remodeling. This framework will be used to investigate the mechanisms that contribute to disease states, as well as the relevant stimuli in growth and remodeling. The ultimate goal is to create a framework that can be used to aid in the identification and prediction of therapies (mechanical or pharmaceutical) to aid in clinical care.

References

Ait-Mou, Y., Hsu, K., Farman, G. P., Kumar, M., Greaser, M. L., Irving, T. C., & de Tombe, P. P. (2016). Titin strain contributes to the Frank-Starling law of the heart by structural rearrangements of both thin- and thick-filament proteins. *Proc Natl Acad Sci U S A, 113*(8), 2306-2311. doi:10.1073/pnas.1516732113

Alastrue, V., Pena, E., Martinez, M. A., & Doblare, M. (2007). Assessing the use of the "opening angle method" to enforce residual stresses in patient-specific arteries. *Ann Biomed Eng, 35*(10), 1821-1837. doi:10.1007/s10439-007-9352-4

Baylor, S. M., & Hollingworth, S. (2003). Sarcoplasmic reticulum calcium release compared in slow-twitch and fast-twitch fibres of mouse muscle. *J Physiol, 551*(Pt 1), 125-138. doi:10.1113/jphysiol.2003.041608

Burkhoff, D., Mirsky, I., & Suga, H. (2005). Assessment of systolic and diastolic ventricular properties via pressure-volume analysis: a guide for clinical, translational, and basic researchers. *Am J Physiol Heart Circ Physiol, 289*(2), H501-512. doi:10.1152/ajpheart.00138.2005

Campbell, K. S. (2014). Dynamic coupling of regulated binding sites and cycling myosin heads in striated muscle. *J Gen Physiol, 143*(3), 387-399. doi:10.1085/jgp.201311078

Campbell, K. S. (2016). Compliance Accelerates Relaxation in Muscle by Allowing Myosin Heads to Move Relative to Actin. *Biophys J, 110*(3), 661-668. doi:10.1016/j.bpj.2015.12.024

Campbell, K. S., Chrisman, B. S., & Campbell, S. G. (2020). Multiscale Modeling of Cardiovascular Function Predicts That the End-Systolic Pressure Volume Relationship Can Be Targeted via Multiple Therapeutic Strategies. *Front Physiol, 11*, 1043. doi:10.3389/fphys.2020.01043

Campbell, K. S., Janssen, P. M. L., & Campbell, S. G. (2018). Force-Dependent Recruitment from the Myosin Off State Contributes to Length-Dependent Activation. *Biophys J, 115*(3), 543-553. doi:10.1016/j.bpj.2018.07.006

Campbell, K. S., Yengo, C. M., Lee, L. C., Kotter, J., Sorrell, V. L., Guglin, M., & Wenk, J. F. (2019). Closing the therapeutic loop. *Arch Biochem Biophys, 663*, 129-131. doi:10.1016/j.abb.2019.01.006

Chung, C. S., Hoopes, C. W., & Campbell, K. S. (2017). Myocardial relaxation is accelerated by fast stretch, not reduced afterload. *J Mol Cell Cardiol, 103*, 65-73. doi:10.1016/j.yjmcc.2017.01.004

Clark, J. A., Sewanan, L. R., Schwan, J., Kluger, J., Campbell, K. S., & Campbell, S. G. (2021). Fast-relaxing cardiomyocytes exert a dominant role in the relaxation behavior of heterogeneous myocardium. *Arch Biochem Biophys, 697*, 108711. doi:10.1016/j.abb.2020.108711

de Tombe, P. P., & Stienen, G. J. (2007). Impact of temperature on cross-bridge cycling kinetics in rat myocardium. *J Physiol, 584*(Pt 2), 591-600. doi:10.1113/jphysiol.2007.138693

Finocchiaro, G., Sheikh, N., Leone, O., Westaby, J., Mazzarotto, F., Pantazis, A., . . . Olivotto, I. (2021). Arrhythmogenic potential of myocardial disarray in

hypertrophic cardiomyopathy: genetic basis, functional consequences and relation to sudden cardiac death. *Europace*. doi:10.1093/europace/euaa348

Fukuda, N., Sasaki, D., Ishiwata, S., & Kurihara, S. (2001). Length dependence of tension generation in rat skinned cardiac muscle: role of titin in the Frank-Starling mechanism of the heart. *Circulation, 104*(14), 1639-1645. doi:10.1161/hc3901.095898

Genet, M., Rausch, M. K., Lee, L. C., Choy, S., Zhao, X., Kassab, G. S., . . . Kuhl, E. (2015). Heterogeneous growth-induced prestrain in the heart. *J Biomech, 48*(10), 2080-2089. doi:10.1016/j.jbiomech.2015.03.012

Geuzaine, C., & Remacle, J.-F. (2009). Gmsh: A 3-D finite element mesh generator with built-in pre- and post-processing facilities. *International Journal for Numerical Methods in Engineering, 79*(11), 1309-1331. doi:https://doi.org/10.1002/nme.2579

Gonzalez, E., Messi, M. L., & Delbono, O. (2000). The specific force of single intact extensor digitorum longus and soleus mouse muscle fibers declines with aging. *J Membr Biol, 178*(3), 175-183. doi:10.1007/s002320010025

Guccione, J. M., & McCulloch, A. D. (1993). Mechanics of active contraction in cardiac muscle: Part I--Constitutive relations for fiber stress that describe deactivation. *J Biomech Eng, 115*(1), 72-81.

Guccione, J. M., Waldman, L. K., & McCulloch, A. D. (1993). Mechanics of active contraction in cardiac muscle: Part II--Cylindrical models of the systolic left ventricle. *J Biomech Eng, 115*(1), 82-90.

Hill, A. V. (1938). The heat of shortening and the dynamic constants of muscle. *Proc. R. Soc. Lond., 126*, 136-195.

Hunter, P. J., McCulloch, A. D., & ter Keurs, H. E. (1998). Modelling the mechanical properties of cardiac muscle. *Prog Biophys Mol Biol, 69*(2-3), 289-331.

Huxley, A. F. (1957). Muscle structure and theories of contraction. *Prog Biophys Biophys Chem, 7*, 255-318.

Huxley, H. E., Stewart, A., Sosa, H., & Irving, T. (1994). X-ray diffraction measurements of the extensibility of actin and myosin filaments in contracting muscle. *Biophys J, 67*(6), 2411-2421. doi:10.1016/S0006-3495(94)80728-3

Kampourakis, T., Ponnam, S., & Irving, M. (2018). Hypertrophic cardiomyopathy mutation R58Q in the myosin regulatory light chain perturbs thick filament-based regulation in cardiac muscle. *J Mol Cell Cardiol, 117*, 72-81. doi:10.1016/j.yjmcc.2018.02.009

Kampourakis, T., Sun, Y. B., & Irving, M. (2016). Myosin light chain phosphorylation enhances contraction of heart muscle via structural changes in both thick and thin filaments. *Proc Natl Acad Sci U S A, 113*(21), E3039-3047. doi:10.1073/pnas.1602776113

Konstam, M. A., & Abboud, F. M. (2017). Ejection Fraction: Misunderstood and Overrated (Changing the Paradigm in Categorizing Heart Failure). *Circulation, 135*(8), 717-719. doi:10.1161/CIRCULATIONAHA.116.025795

Kroon, W., Delhaas, T., Bovendeerd, P., & Arts, T. (2009). *Adaptive Reorientation of Cardiac Myofibers: Comparison of Left Ventricular Shear in Model and Experiment*, Berlin, Heidelberg.

Land, S., & Niederer, S. A. (2015). A Spatially Detailed Model of Isometric Contraction Based on Competitive Binding of Troponin I Explains Cooperative Interactions

between Tropomyosin and Crossbridges. *PLoS Comput Biol, 11*(8), e1004376. doi:10.1371/journal.pcbi.1004376

Laurita, K. R., & Singal, A. (2001). Mapping action potentials and calcium transients simultaneously from the intact heart. *Am J Physiol Heart Circ Physiol, 280*(5), H2053-2060. doi:10.1152/ajpheart.2001.280.5.H2053

Logg, A., Mardal, K.-A. & Wells, G. (2012). *Automated solution of differential equations by the finite element method: The FEniCS book*: Springer Science & Business Media.

Mamidi, R., Gresham, K. S., & Stelzer, J. E. (2014). Length-dependent changes in contractile dynamics are blunted due to cardiac myosin binding protein-C ablation. *Front Physiol, 5*, 461. doi:10.3389/fphys.2014.00461

Mann, C. K., Lee, L. C., Campbell, K. S., & Wenk, J. F. (2020). Force-dependent recruitment from myosin OFF-state increases end-systolic pressure-volume relationship in left ventricle. *Biomech Model Mechanobiol*. doi:10.1007/s10237-020-01331-6

Marcucci, L., Washio, T., & Yanagida, T. (2017). Titin-mediated thick filament activation, through a mechanosensing mechanism, introduces sarcomere-length dependencies in mathematical models of rat trabecula and whole ventricle. *Sci Rep, 7*(1), 5546. doi:10.1038/s41598-017-05999-2

Martinsson, T., Oldfors, A., Darin, N., Berg, K., Tajsharghi, H., Kyllerman, M., & Wahlstrom, J. (2000). Autosomal dominant myopathy: missense mutation (Glu-706 --> Lys) in the myosin heavy chain IIa gene. *Proc Natl Acad Sci U S A, 97*(26), 14614-14619. doi:10.1073/pnas.250289597

Olah, A., Nemeth, B. T., Matyas, C., Horvath, E. M., Hidi, L., Birtalan, E., . . . Radovits, T. (2015). Cardiac effects of acute exhaustive exercise in a rat model. *Int J Cardiol, 182*, 258-266. doi:10.1016/j.ijcard.2014.12.045

Pacher, P., Nagayama, T., Mukhopadhyay, P., Batkai, S., & Kass, D. A. (2008). Measurement of cardiac function using pressure-volume conductance catheter technique in mice and rats. *Nat Protoc, 3*(9), 1422-1434. doi:10.1038/nprot.2008.138

Pulcastro, H. C., Awinda, P. O., Methawasin, M., Granzier, H., Dong, W., & Tanner, B. C. (2016). Increased Titin Compliance Reduced Length-Dependent Contraction and Slowed Cross-Bridge Kinetics in Skinned Myocardial Strips from Rbm (20DeltaRRM) Mice. *Front Physiol, 7*, 322. doi:10.3389/fphys.2016.00322

Rice, J. J., Wang, F., Bers, D. M., & de Tombe, P. P. (2008). Approximate model of cooperative activation and crossbridge cycling in cardiac muscle using ordinary differential equations. *Biophys J, 95*(5), 2368-2390. doi:10.1529/biophysj.107.119487

Rodriguez, E. K., Hoger, A., & McCulloch, A. D. (1994). Stress-dependent finite growth in soft elastic tissues. *J Biomech, 27*(4), 455-467. doi:10.1016/0021-9290(94)90021-3

Schneider, N. S., Shimayoshi, T., Amano, A., & Matsuda, T. (2006). Mechanism of the Frank-Starling law--a simulation study with a novel cardiac muscle contraction model that includes titin and troponin I. *J Mol Cell Cardiol, 41*(3), 522-536. doi:10.1016/j.yjmcc.2006.06.003

Shavik, S. M., Wall, S. T., Sundnes, J., Burkhoff, D., & Lee, L. C. (2017). Organ-level validation of a cross-bridge cycling descriptor in a left ventricular finite element model: effects of ventricular loading on myocardial strains. *Physiol Rep, 5*(21). doi:10.14814/phy2.13392

Shoucri, R. M., & Kohar, R. (2012). Criteria for study of heart failure derived from ESPVR. *Conf Proc IEEE Eng Med Biol Soc, 2012*, 5586-5589. doi:10.1109/EMBC.2012.6347260

Skalak, R., Zargaryan, S., Jain, R. K., Netti, P. A., & Hoger, A. (1996). Compatibility and the genesis of residual stress by volumetric growth. *J Math Biol, 34*(8), 889-914. doi:10.1007/BF01834825

Spottiswoode, B. S., Zhong, X., Hess, A. T., Kramer, C. M., Meintjes, E. M., Mayosi, B. M., & Epstein, F. H. (2007). Tracking myocardial motion from cine DENSE images using spatiotemporal phase unwrapping and temporal fitting. *IEEE Trans Med Imaging, 26*(1), 15-30. doi:10.1109/TMI.2006.884215

Tajima, Y., Makino, K., Hanyuu, T., Wakabayashi, K., & Amemiya, Y. (1994). X-ray evidence for the elongation of thin and thick filaments during isometric contraction of a molluscan smooth muscle. *J Muscle Res Cell Motil, 15*(6), 659-671.

Trayanova, N. A., & Rice, J. J. (2011). Cardiac electromechanical models: from cell to organ. *Front Physiol, 2*, 43. doi:10.3389/fphys.2011.00043

Xi, C., Kassab, G. S., & Lee, L. C. (2019). Microstructure-based finite element model of left ventricle passive inflation. *Acta Biomater, 90*, 241-253. doi:10.1016/j.actbio.2019.04.016

Zhang, X., Haynes, P., Campbell, K. S., & Wenk, J. F. (2015). Numerical evaluation of myofiber orientation and transmural contractile strength on left ventricular function. *J Biomech Eng, 137*(4), 044502. doi:10.1115/1.4028990

Zhang, X., Liu, Z.-Q., Campbell, K. S., & Wenk, J. F. (2018). Evaluation of a Novel Finite Element Model of Active Contraction in the Heart. *Frontiers in Physiology, 9*(425). doi:10.3389/fphys.2018.00425

Zhang, X., Liu, Z. Q., Singh, D., Wehner, G. J., Powell, D. K., Campbell, K. S., . . . Wenk, J. F. (2017). Regional quantification of myocardial mechanics in rat using 3D cine DENSE cardiovascular magnetic resonance. *NMR Biomed, 30*(8). doi:10.1002/nbm.3733

Zimmerman, S. D., Criscione, J., & Covell, J. W. (2004). Remodeling in myocardium adjacent to an infarction in the pig left ventricle. *Am J Physiol Heart Circ Physiol, 287*(6), H2697-2704. doi:10.1152/ajpheart.00160.2004

Vita

Charles Kurtis Mann

<u>Education</u>

Georgetown College, Georgetown, KY

- Bachelor of Science in Mathematics   2014

<u>Scholastic Honors/Awards</u>

Halcomb Fellowship in Medicine and Engineering, University of Kentucky   2018 - 2020

<u>Publications</u>

Sharifi, H, Mann, C. K., Rockward, A., Mehri, M., Mojumder, J., Lee, L. C., Campbell, K. S., Wenk, J. F. (2021). Multiscale Simulations of Cardiac Growth and Remodeling. Accepted for publication in Biophysical Reviews.

Mann, C. K., Sharifi, H., Rockward, A., Mojumder, J., Lee, L. C., Campbell, K. S., Wenk, J. F. Myofibril Disarray Decreases Peak Stress & Efficiency in A Finite Element Model of Muscle Fiber [abstract]. In: Summer Biomechanics, Bioengineering and Biotransport Conference Proceedings Book 2021; June 14-18, 2021. Abstract 338.

Mann, C. K., Lee, L. C., Campbell, K. S., & Wenk, J. F. (2020). Force-dependent recruitment from myosin OFF-state increases end-systolic pressure-volume relationship in left ventricle. *Biomech Model Mechanobiol.* doi:10.1007/s10237-020-01331-6

Mann, C. K., Liu, Z., Zhang, X., Campbell, K. S., Wenk, J.F. Recruitment from Myosin Off State Steepens ESPVR in Finite Element Model of Left Ventricle [abstract]. In Biophysical Journal Vol. 116Issue 3Supplementp30a; February 15, 2019. Abstract 153-Plat